



# Turbulent mixing and nuclear burning in stellar interiors

Miroslav Mocák,<sup>1</sup>★ Casey Meakin,<sup>1,2,3</sup> Simon W. Campbell,<sup>4,5</sup> and W. David Arnett<sup>3</sup>

<sup>1</sup>Theoretical Division, LANL, Los Alamos, NM 87545, USA

<sup>2</sup>Karagozian & Case, Inc., Glendale, CA 91203, USA

<sup>3</sup>Steward Observatory, University of Arizona, Tucson, AZ 85721, USA

<sup>4</sup>Monash Centre for Astrophysics, School of Physics and Astronomy, Monash University, Clayton 3800, Australia

<sup>5</sup>Max-Planck-Institut für Astrophysik (MPA), D-85748 Garching, Germany

Accepted 2018 August 31. Received 2018 August 20; in original form 2017 October 14

## ABSTRACT

The turbulent burning of nuclei is a common phenomenon in the evolution of stars. Here we examine a challenging case: the merging of the neon and oxygen burning shells in a  $23\text{ M}_\odot$  star. A previously unknown quasi-steady state is established by the interplay between mixing, turbulent transport, and nuclear burning. The resulting stellar structure has two burning shells *within a single convection zone*. We find that the new neon burning layer covers an extended region of the convection zone, with the burning peak occurring substantially below where the average convective turnover timescale becomes equal to the burning timescale. These characteristics differ from those predicted by 1D stellar evolution models of similar ingestion events. We develop the mean-field turbulence equations that govern compositional evolution, and use them to interpret our data set. An important byproduct is a means to quantify sub-grid-scale effects intrinsic to the numerical hydrodynamic scheme. For implicit large eddy simulations, the analysis method is particularly powerful because it can reveal where and how simulated flows are modified by resolution, and provide straightforward physical interpretations of the effects of dissipation or induced transport. Focusing on the mean-field composition variance equations for our analysis, we recover a Kolmogorov rate of turbulent dissipation without it being imposed, in agreement with previous results which used the turbulent kinetic energy equation.

**Key words:** hydrodynamics – turbulence – stars: evolution – stars: interiors.

## 1 INTRODUCTION

It is now feasible to simulate stellar convection in three-dimensions (3D), with realistic microphysics, multiple species of nuclei, and sufficient resolution in space and time to represent turbulent flow (Meakin & Arnett 2007; Mocák, Siess & Müller 2011; Woodward, Herwig & Lin 2013). Historical work on stellar convection (Böhm-Vitense 1958) and 3D simulations of stellar atmospheres (Stein & Nordlund 1998) have generally focused on flows having uniform composition, a case which is usually appropriate for the outer layers of stars.

By contrast convection in stellar interiors is generally characterized by nuclear burning and nonuniform composition. Here, we examine the interaction between turbulent convection, thermonuclear burning, and entrainment at boundaries. Simulations of convective shells, driven by nuclear burning, show entrainment

of material from surrounding stable layers. Erosion at boundaries introduces inhomogeneities in composition, entropy, and buoyancy into the convective flow. This can be viewed as a multi-stage process of entrainment, transport, dispersion (or stirring) induced from the largest to smallest eddies, as well as diffusion, spanning the full spectrum of space-time-scales of the flow (Dimotakis 2005). The feedback of such mixing on nuclear burning, convection, and its impact on the evolution of the star remains largely unexplored: an ad hoc diffusion operator is almost universally used in stellar evolution. This paper begins to analyse these stages.

We focus on the oxygen burning shell in a massive supernova progenitor. Oxygen burning and neon burning occur at sufficiently similar temperatures that these burning shells may interact (Arnett 1974a; Arnett 1974b). Interaction was indeed found in the 3D simulations of Meakin (2006) and Meakin & Arnett (2007), but was not analysed in detail there. Here, we present a detailed account of the compositional mixing and modified nuclear burning, which occurs as the convective oxygen-burning shell merges with the (initially) stable overlying neon shell.

\* E-mail: [miroslav.mocak@gmail.com](mailto:miroslav.mocak@gmail.com) (MM); [casey.meakin@gmail.com](mailto:casey.meakin@gmail.com) (CM)

We use 3D numerical hydrodynamics in the implicit large eddy simulation framework ILES (Grinstein, Margolin & Rider 2007), which means we solve the Euler equations with a non-oscillatory finite volume numerical fluid solver. In the current study we use the PPM method (Colella & Woodward 1984). The dissipation in such solvers comes from solving the Riemann shock problem over each zone  $\Delta_s$ , giving a dissipation rate<sup>1</sup> of  $\sim v_s^3/\Delta_s$  as a shock of speed  $v_s$  traverses a zone. In a turbulent cascade the mean damping is  $\mathcal{D} \sim v_s^3/\Delta_s \sim v^3/\ell$ , which is determined by the rms velocity  $v$  and dimension  $\ell$  of the turbulent region. Use of such solvers introduces an implicit sub-grid model which corresponds to a Kolmogorov turbulent cascade, freeing computational resources to capture the large-scales relevant to astrophysics. See Grinstein et al. (2007) for references and a more rigorous discussion.

This is in contrast to the direct numerical simulation approach DNS (Pope 2000), which solves the Navier–Stokes difference equations on the grid, all the way down to the dissipation scale. In this approach, most of the computational effort is spent on these small scales, which are buried in the turbulent cascade. Sytine et al. (2000) showed that both methods converge to the same result, but that ILES is more efficient for highly turbulent flows. We have confirmed that our simulations extend from the integral (large) scale down into the inertial range of the turbulent cascade (e.g. Cristini et al. 2017).

In this paper, we extend our analysis by using an approach inspired by Reynolds-averaged Navier–Stokes (RANS) methods (Viallet et al. 2013; Mocák et al. 2014; Arnett et al. 2015). Our approach differs from traditional RANS (Besnard et al. 1992; Chassaing et al. 2010) in two fundamental ways: (1) the fluctuations are taken from our simulations, and hence are dynamically constrained, and (2) we solve the ILES Euler equations. A more accurate acronym than ‘RANS’ (which we have used previously) is needed for clarity; we choose ‘Reynolds-averaged ILES’ (RA-ILES), to distinguish our approach. Unlike unconstrained RANS analysis, our RA-ILES equations are complete, exact to the accuracy of our grid, and require little added computational cost. There is no closure issue.<sup>2</sup>

Previous papers (Meakin & Arnett 2007; Viallet et al. 2013; Arnett et al. 2015; Cristini et al. 2017) have focused on the turbulent kinetic energy equation (TKE); here our analysis shifts to mean-field transport equations for the density of  $^{16}\text{O}$  and  $^{20}\text{Ne}$ , and their turbulent fluxes and variances, complemented by analysis of relevant time-scales and nuclear burning processes. These transport equations are the ones which deal with changes in composition variance: i.e. mixing.

The paper is organized as follows: In Section 2, we describe the initial conditions and the 3D stellar model that we investigate in this paper. In Section 3, we develop the RA-ILES equations used for our analysis. In Section 4, we define several time-scales which we use to characterize physical processes operating in the simulated flow. In Section 5, we present the results from our RA-ILES analysis of oxygen and neon entrainment, transport, dissipation, and burning. We use the composition-related mean-field equations and provide a

systematic description of each term in the budget equations with an emphasis placed on physical interpretation. We then look at effects of resolution on our results in Section 5.4. Finally, we conclude with a summary and discussion in Section 6.

## 2 INITIAL MODEL AND SIMULATION METHOD

The initial 1D model for our 3D simulation is a  $23\,\text{M}_\odot$  supernova progenitor. It was evolved with the 1D TYCHO stellar evolution code (Young & Arnett 2005; Arnett, Meakin & Young 2010) using mixing-length theory (MLT) to a point just following core oxygen burning where oxygen, neon, carbon, helium, and hydrogen are burning in concentric shells outside a degenerate core of silicon and sulfur. The structure of the 1D initial model is shown in the panels of the top row of Fig. 1. It has a single convective oxygen shell enclosed by two stable layers. The initial convective region is driven primarily by nuclear burning of oxygen and extends from its base around  $4.3 \times 10^8\,\text{cm}$  up to a radius around  $7.2 \times 10^8\,\text{cm}$ , where the Ledoux criterion indicates a stable boundary. The stable layers below and above are composed primarily of silicon and oxygen; in the top layer the dominant nuclear burning is that of neon, and nonconvective. Such stellar structures are quite common and can be found, e.g. in cores of low-mass red giants during the core helium flash, or during core carbon flashes of ‘super-AGB’ stars (Mocák, Müller & Siess 2012).

Reactive-hydrodynamic evolution in 3D was computed with the PROMPI code, a version of the legacy PROMETHEUS code (Fryxell, Arnett & Mueller 1991) adapted to parallel computing via the Message Passing Interface (MPI). This code is an Eulerian implementation of the piecewise parabolic method (PPM) of Colella & Woodward (1984) updated with a Riemann solver for real gases according to Colella & Glaz (1985). Additional added physics include self gravity in the spherically symmetric approximation, a realistic equation of state to handle the semi-degenerate stellar plasma (Timmes & Swesty 2000), and a general nuclear reaction network. For the current simulation we use a 25-isotope network that includes neutrons, protons,  $^4\text{He}$ ,  $^{12}\text{C}$ ,  $^{16}\text{O}$ ,  $^{20}\text{Ne}$ ,  $^{23}\text{Na}$ ,  $^{24}\text{Mg}$ ,  $^{28}\text{Si}$ ,  $^{31}\text{P}$ ,  $^{32}\text{S}$ ,  $^{34}\text{S}$ ,  $^{35}\text{Cl}$ ,  $^{36}\text{Ar}$ ,  $^{38}\text{Ar}$ ,  $^{39}\text{K}$ ,  $^{40}\text{Ca}$ ,  $^{42}\text{Ca}$ ,  $^{44}\text{Ti}$ ,  $^{46}\text{Ti}$ ,  $^{48}\text{Cr}$ ,  $^{50}\text{Cr}$ ,  $^{52}\text{Fe}$ ,  $^{54}\text{Fe}$ ,  $^{56}\text{Ni}$ . All of the important strong and weak reactions are included. It is conceptually convenient to decompose the network results into separate processes. In Appendix A we give simpler approximations which are used to identify the different stages of burning.

In the simulation neither Si nor C burning is ever the primary nuclear process. The dominant energy release is due to burning of  $^{16}\text{O}$  and  $^{20}\text{Ne}$ . The dominance of neon burning is the result of entrainment as it mixes  $^{20}\text{Ne}$  into the deeper, hotter layers of the oxygen-burning shell. Oxygen burning is invigorated by mixing in new  $^{16}\text{O}$  fuel from the previously non-convective region (Meakin & Arnett 2007).

We focus on the region encompassing the oxygen- and neon-burning shells and their interactions with each other and with the adjacent stably stratified layers. The computational grid is defined in a spherical coordinate system with periodic boundary conditions in the angular directions and reflecting (non-transmitting) boundaries in the radial directions. The opening angle of the grid is  $27.5^\circ \times 27.5^\circ$  in  $\theta$  and  $\phi$ . A short summary of the simulation properties, including zoning, is presented in Table 1.

Due to its lower computational cost, this medium resolution simulation could be extended over a longer time span than higher resolution simulations, and attain a new and reliable quasi-steady state.

<sup>1</sup>The change in specific kinetic energy over the shock traversal time gives the dissipation rate. PPM approximates sub-grid structure as piece-wise parabolic, smoothing higher order terms and decreasing information (complexity). Variances in velocity and in scalar variables dissipate/diffuse at this same rate at the sub-grid scale.

<sup>2</sup>There is no explicit Navier–Stokes viscosity term to generate higher order moments in the conventional way (Tritton 1988); the implicit turbulent cascade gives closure.

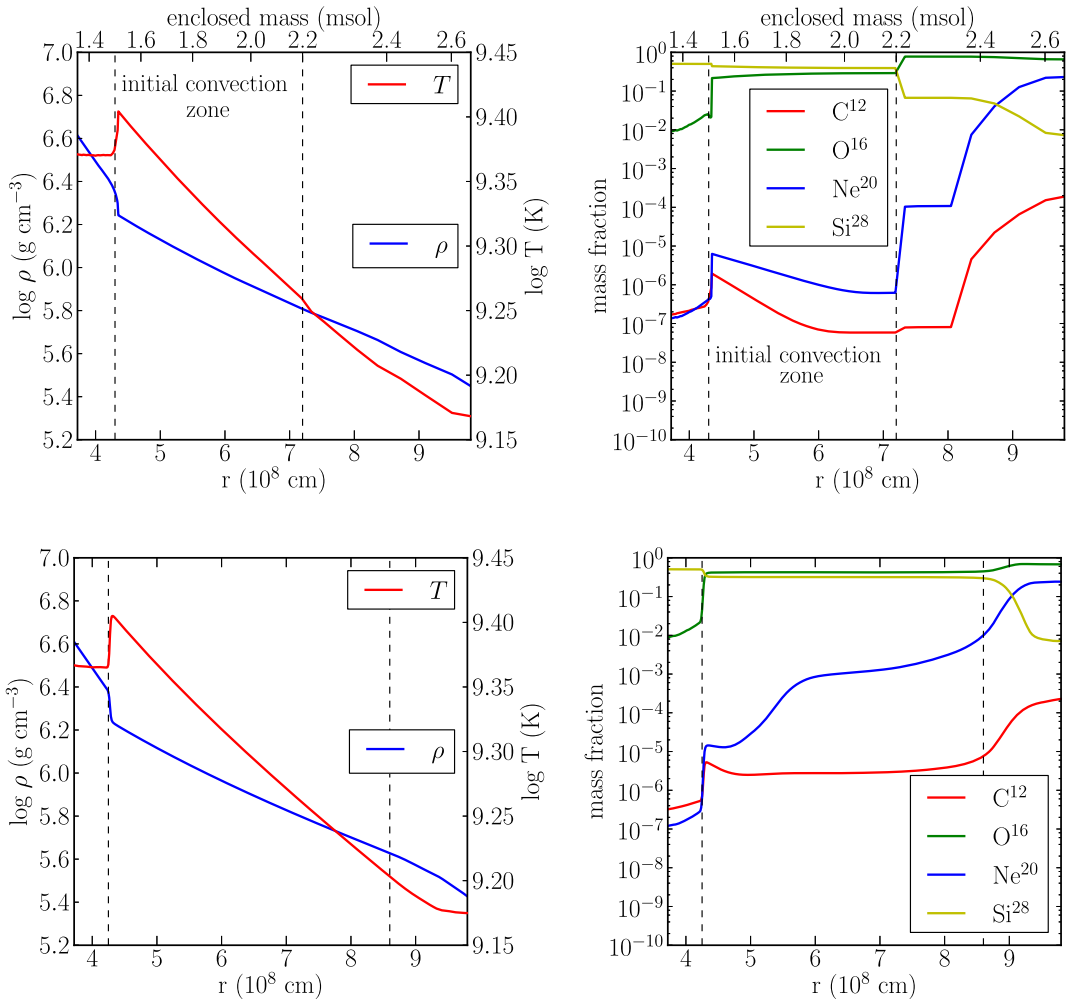


**Figure 1.** Top row: (left) Initial 1D background temperature  $T$  and density  $\rho$ ; and (right) composition profiles (mass fraction). Bottom row: Radial profiles after 300 s of evolution at which point the model has obtained a quasi-steady character. Only the most energetically important nuclear species are shown. Vertical dashed lines mark boundaries of convection.

**Table 1.** 3D oxygen-burning simulation properties (model ob.3d.B).  $\Delta t_{\text{av}}$  is the averaging time-scale for the mean field analysis;  $v_{\text{rms}} = \sqrt{2K_{\text{tot}}/M}$  is the approximate global rms velocity (where  $K_{\text{tot}}$  is the total turbulent kinetic energy in the convection zone and  $M$  mass contained in the convection zone), and  $\tau_{\text{conv}} = 2l_{\text{cvz}}/v_{\text{rms}}$  is the convective turnover time-scale (where  $l_{\text{cvz}}$  is size of the convection zone,  $\sim 4.3 \times 10^8 \text{ cm}$ ). All values were obtained at the central simulation time 1060 s around which we perform all subsequent time-averaging.

Grid dimensions ( $\Delta r, \Delta\theta, \Delta\phi$ )	$6 \times 10^8 \text{ cm} \times 27.5^\circ \times 27.5^\circ$
Grid zoning	$400 \times 100 \times 100$
$\Delta t_{\text{av}}$ (s)	300 s
$v_{\text{rms}}$	$\sim 1.4 \times 10^7 \text{ cm s}^{-1}$
$\tau_{\text{conv}}$	$\sim 65 \text{ s}$

### 3 MEAN-FIELD EVOLUTION EQUATIONS

In this section, we describe and develop the RA-ILES analysis for composition i.e. mean-field equations describing the evolution of mean fields related to composition on spherically averaged shells. The evolution equations for mean composition (Section 3.3), turbulent composition flux (Section 3.4), and composition variance (Section 3.5) are then considered in turn.

### 3.1 Reynolds-averaged ILES analysis

The RA-ILES equations derived here are exact, and do not employ approximations, at least to the extent that the continuum approximation is appropriate and flow features are resolved. This contrasts with methods using closure relationships and truncations of the RANS equations to construct approximate models of turbulence. The RANS equations, when closed by 3D numerical simulations to become ‘RA-ILES’ equations, are able to represent the full range of hydrodynamical behaviour present in a stellar interior.

As shown in Hinze (1975), Besnard et al. (1992), and Chassaing et al. (2010), the RANS framework provides a rational approach to interpreting complex 3D fluid dynamical data. The extension of the methodology to ‘RA-ILES’ (see Section 1) for stellar interiors is discussed in Viallet et al. (2013), Mocák et al. (2014), and Arnett et al. (2015).

### 3.2 The averaging and decomposition procedure

In this section, we define the averaging rules needed to obtain 1D mean and fluctuation fields from 3D flow data. This decomposition makes precise the relationship between the 1D mean fields evolved by a stellar evolution code and 3D hydrodynamic simulations

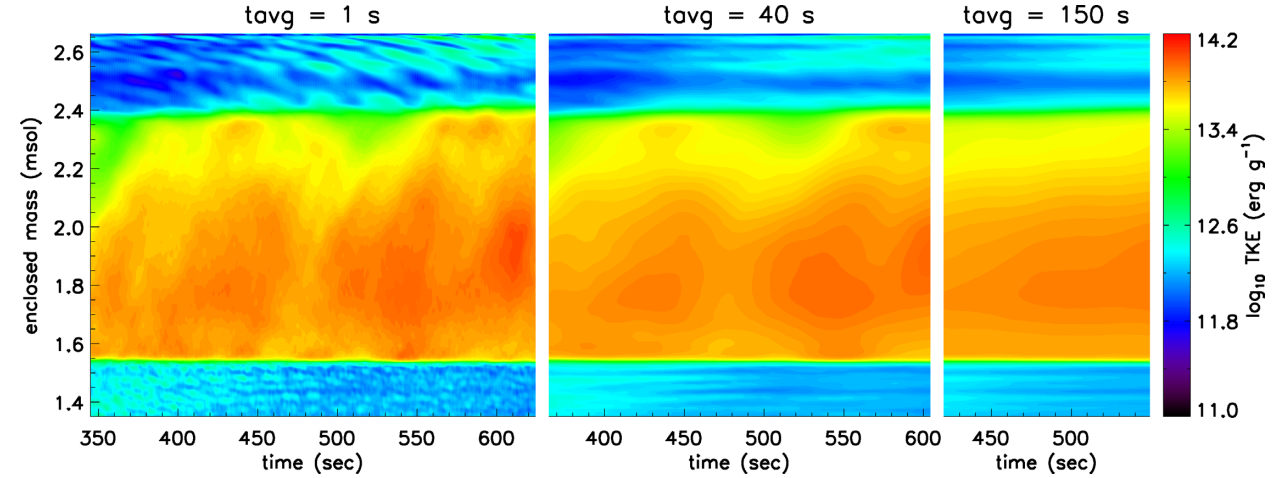


**Figure 2.** Comparison of different averaging windows for turbulent kinetic energy and its resulting mean-field. The purpose of averaging is to separate short time variability, which tends to cancel itself, from more robust long time changes. The left-hand panel illustrates the effect of a short averaging window of 1 s; the turbulent kinetic energy is modulated by convective bursts, and the boundary layers support g-mode waves. The centre panel, with an averaging time of 40 s, shows considerably more smoothing while the right-hand panel, with an averaging time of 150 s, shows no convective bursts, just steady convection.

(Viallet et al. 2013). Two types of averaging are used: in time, and in space. In practice, both types of averaging are combined and contribute to a meaningful average of the flow within a spherical layer by virtue of the ergodic hypothesis<sup>3</sup> and spherical symmetry.<sup>4</sup>

The average of a quantity  $q$  on a spherical shell at radius  $r$  (*i.e.* a mean field) is defined by

$$\bar{q}(r, t_c) = \frac{1}{T \Delta\Omega} \int_{t_c - T/2}^{t_c + T/2} \int_{\Delta\Omega} q(r, \theta, \phi, t') d\Omega dt', \quad (1)$$

where  $d\Omega = \sin\theta d\theta d\phi$  is the solid angle in spherical coordinates,  $T$  is the averaging time period,  $t$  is time and  $\Delta\Omega$  is the solid angle being averaged over. The time coordinate  $t_c$  represents the centre of the time-averaging window used (central time).

Fluctuations, which retain the full time and space dependence as the original, self-consistent 3D flow field, are defined according to the decomposition  $q(\vec{x}, t) = \bar{q}(r, t) + q'(\vec{x}, t)$ , noting that  $\bar{q}'(r, t) = 0$  by construction. Similarly, a Favre (or density weighted) average is given by

$$\tilde{q} = \overline{\rho q} / \overline{\rho}, \quad (2)$$

which defines a complimentary decomposition of the flow according to  $q = \tilde{q} + q''$  where  $q''(r, \theta, \phi, t)$  is referred to as the Favre fluctuation and its mean is zero when Favre averaged:  $\tilde{q}''(r, t) = 0$ . A more complete elaboration on the algebra of these averaging procedures can be found in Chassaing et al. (2010).

The mean fields presented in this paper were calculated by post-processing snapshots (that were written to disc every 0.5 s of simulated time, for a period from 888 s up to 1211 s), by following these steps:

<sup>3</sup>An average of a physical quantity over a statistical ensemble is equivalent to its average over time.

<sup>4</sup>If spherical symmetry were broken, as it would be in the presence of a magnetic field or a mean stellar rotation field, spherical averaging would not be appropriate. In the case of a mild rotation field, for example, mean fields could not be restricted to less than two dimensions and would be represented most naturally in a meridional plane.

(i) Calculate Reynolds fluctuations for each snapshot, at time  $t$ , from the raw 3D simulation data, as defined above:

$$q'_{\text{inst}}(r, \theta, \phi, t) = q(r, \theta, \phi, t) - \langle q \rangle(r, t), \quad (3)$$

where the dependence on space and time variables are shown for each term.  $\langle q \rangle(r, t) = 1/\Delta\Omega \int_{\Delta\Omega} q(r, \theta, \phi, t) d\Omega$  gives spatial average of  $q$  for a given time  $t$  and radius  $r$ .

(ii) Calculate needed products of any required thermodynamic quantities  $q_1, q_2, q_3$ , etc. (for example  $q'_1 q_3$  or  $q'_1 q''_2 q''_3$ ) from 3D fields. Favre fluctuation can be obtained from

$$q''_{\text{inst}} = q'_{\text{inst}} - \frac{\langle \rho q'_{\text{inst}} \rangle}{\langle \rho \rangle}. \quad (4)$$

(iii) space and time average the products calculated in the prior step around central time  $t_c$  as defined in equation (1) above.

We find that the turbulent flow can be very well sampled when using an averaging time window of width  $T$  around two convective turnover time-scales (Mocák et al. 2014). Fig. 2 shows an example of the averaging window effect on our flow for the mean specific turbulent kinetic energy (TKE) defined as  $\tilde{k} = \frac{1}{2}(\widetilde{u_r'' u_r''} + \widetilde{u_\theta'' u_\theta''} + \widetilde{u_\phi'' u_\phi''})$ , where  $u_i$  are components of the velocity field. Small time-scale features are absorbed into the mean-field when the averaging window exceeds around 150 seconds ( $\sim 2$  turnover times). In order to present a robust statistical analysis we use an averaging window of 300 s throughout this paper, which is  $\sim 4$  turnover times.

### 3.3 Evolution equation for mean composition

The instantaneous evolution equation for mass fraction of element  $i$  in spherical geometry is Arnett (1996, equation 4.97),

$$\partial_t (\rho X_i) = -\nabla \cdot (\rho \mathbf{u} X_i) + \rho \dot{X}_i^{\text{nuc}}. \quad (5)$$

Applying our decomposition and averaging procedure (Section 3.2), we obtain the following 1D transport equation

$$\tilde{\rho} \tilde{D}_t \tilde{X}_i = -\nabla_r f_i + \tilde{\rho} \dot{\tilde{X}}_i^{\text{nuc}} + \mathcal{N}_i, \quad (6)$$

where  $X_i$  is mass fraction of chemical element  $i$ ,  $\rho$  is density,  $\mathbf{u} = [u_r, u_\theta, u_\phi]$  is the velocity vector,  $\nabla$  is the divergence operator,  $\dot{X}_i^{\text{nuc}}$  is the rate of nuclear burning of  $i$ , and  $f_i = \widetilde{\rho X_i'' u_r''}$  is the

turbulent flux of element  $i$ .  $\nabla_r(\cdot) = (1/r^2)\partial_r r^2(\cdot)$  is the radial divergence operator and the  $\tilde{D}_t$  is the mean-flow Lagrangian derivative  $\tilde{D}_t(\cdot) = \partial_t(\cdot) + \tilde{u}_n \partial_n(\cdot)$ .

The mean-field transport equation (equation 6) states that the temporal change of mass fraction of an element  $i$  in the Lagrangian frame of reference,  $\bar{\rho} \tilde{D}_t \tilde{X}_i$ , is caused by either a spatial redistribution by the turbulent flux,  $-\nabla_r f_i$ ; or by nuclear burning,  $\bar{\rho} \tilde{X}_i^{\text{nuc}}$ .

We define the numerical residual in these equations by  $\mathcal{N}_i$ , which represents the implicit action of the numerical simulation algorithm. These terms are discussed in more detail in the following sections and again later in Section 5.

### 3.4 Evolution equation for turbulent composition flux

The transport equation for the turbulent flux of an arbitrary chemical element can be obtained by using the following general formula for second-order moments (Mocák et al. 2014),

$$\begin{aligned} \bar{\rho} \tilde{D}_t c'' d'' &= +\bar{c}'' \bar{\rho} \bar{D}_t \bar{d} - \bar{\rho} \bar{c}'' \bar{u}_n'' \bar{\partial}_n \bar{d} \\ &\quad + \bar{d}'' \bar{\rho} \bar{D}_t \bar{c} - \bar{\rho} \bar{d}'' \bar{u}_n'' \bar{\partial}_n \bar{c} - \bar{\partial}_n \bar{\rho} \bar{c}'' \bar{d}'' \bar{u}_n'' \end{aligned} \quad (7)$$

by substituting  $X_i$  for  $c$  and  $u_r$  for  $d$  and using the radial momentum equation

$$\rho D_t(u_r) = \nabla \cdot \tau_r - G_r^M - \partial_r P + \rho g_r, \quad (8)$$

where  $\tau_r = [\tau_{rr}, \tau_{r\theta}, \tau_{r\phi}]$  contains the radial components of the viscous stress tensor (not explicitly included in our simulation model),  $G_r^M = -(\rho u_\theta^2 - \tau_{\theta\theta})/r - (\rho u_\phi^2 - \tau_{\phi\phi})/r$  is a geometric term,  $P$  is the pressure, and  $g_r$  is the gravitational acceleration in the radial direction.

After averaging, we arrive at the flux evolution equation

$$\begin{aligned} \bar{\rho} \tilde{D}_t(f_i/\bar{\rho}) &= -\nabla_r f_i - f_i \bar{\partial}_r \tilde{u}_r - \tilde{R}_{rr} \bar{\partial}_r \tilde{X}_i - \bar{X}_i'' \bar{\partial}_r \bar{P} \\ &\quad - \bar{X}_i'' \bar{\partial}_r \bar{P}' + \bar{u}_r'' \bar{\rho} \bar{X}_i^{\text{nuc}} + \mathcal{G}_i + \mathcal{N}_{f_i}, \end{aligned} \quad (9)$$

where  $f_i^r = \bar{\rho} \bar{X}_i'' \bar{u}_r'' \bar{u}_r''$  is the radial component of the ‘flux of the turbulent flux’ of element  $i$ . Here,  $-f_i \bar{\partial}_r \tilde{u}_r$  is a production term due to velocity effects controlled by the flux itself. The  $-\tilde{R}_{rr} \bar{\partial}_r \tilde{X}_i$  term is a production term which transports the flux from regions with higher  $X_i$  to regions with lower  $X_i$  or vice versa and is controlled by the Reynolds stress  $\tilde{R}_{rr} = \bar{\rho} \bar{u}_r'' \bar{u}_r''$ . The terms  $-\bar{X}_i'' \bar{\partial}_r \bar{P}$  and  $\bar{X}_i'' \bar{\partial}_r \bar{P}'$  drive evolution of the flux in the presence of a pressure gradient and pressure fluctuations. The term  $+\bar{u}_r'' \bar{\rho} \bar{X}_i$  drives the evolution of the flux by the net nuclear burning of element  $i$ . Finally, the term  $\mathcal{G}_i = \bar{G}_i^r - \bar{X}_i'' \bar{G}_r^M$ , where  $\bar{G}_i^r = -\bar{\rho} \bar{X}_i'' \bar{u}_\theta'' \bar{u}_\theta''/r - \bar{\rho} \bar{X}_i'' \bar{u}_\phi'' \bar{u}_\phi''/r$  mediates the production of  $f_i$  due to centrifugal forces caused by horizontal (non-radial) motion of the flow. The equation contains additionally a term  $\bar{X}_i'' \bar{\rho} g_r$  term, which we neglect due to gravitational acceleration  $g_r$  being constant in the simulation.

The residuals of all these mean fields in the flux transport equation,  $\mathcal{N}_{f_i}$ , represent numerical effects which we do not calculate explicitly in RA-ILES, which has no explicit viscous (Navier–Stokes) term. Their magnitude is determined solely by the implicit action of our numerical scheme at the sub-grid scale. The precise mathematical formulation of the term is following:

$$\mathcal{N}_{f_i} = -\nabla_r(\bar{X}_i'' \bar{\tau}_{rr}) + \varepsilon_i^\tau + \mathcal{G}_i^\tau, \quad (10)$$

where

$$\begin{aligned} \varepsilon_i^\tau &= -\bar{\tau}_{rr} \bar{\partial}_r \bar{X}_i'' - \bar{\tau}_{r\theta}(1/r) \bar{\partial}_\theta \bar{X}_i'' - \bar{\tau}_{r\phi}(1/r \sin \theta) \bar{\partial}_\phi \bar{X}_i'' \\ \mathcal{G}_i^\tau &= +\bar{X}_i'' \bar{\tau}_{\theta\theta} \bar{\tau}_{\theta\theta}/r + \bar{X}_i'' \bar{\tau}_{\phi\phi} \bar{\tau}_{\phi\phi}/r. \end{aligned}$$

The term  $-\nabla_r(\bar{X}_i'' \bar{\tau}_{rr})$  is a flux of a composition flux controlled by viscosity;  $\varepsilon_i^\tau$  is a viscous dissipation of the turbulent flux, and  $\mathcal{G}_i^\tau$  is of geometric origin and contributes to flux production due to action of viscosity.

### 3.5 Evolution equation for composition variance

To derive a transport equation for the variance of composition fluctuations of an arbitrary element  $i$ , we use equation (7) and substitute  $c$  for  $d$ :

$$\bar{\rho} \tilde{D}_t \bar{c}'' \bar{c}'' = +2\bar{c}'' \bar{\rho} \bar{D}_t \bar{c} - 2\bar{\rho} \bar{c}'' \bar{u}_n'' \bar{\partial}_n \bar{c} - \bar{\partial}_n \bar{\rho} \bar{c}'' \bar{c}'' \bar{u}_n''. \quad (11)$$

Next, we substitute a mass fraction of a given element  $X_i$  for  $c$  and find

$$\bar{\rho} \tilde{D}_t \sigma_i = -\nabla_r f_i^\sigma - 2f_i \bar{\partial}_r \tilde{X}_i + 2\bar{X}_i'' \bar{\rho} \bar{X}_i^{\text{nuc}} + \mathcal{N}_{\sigma_i}, \quad (12)$$

where  $\sigma_i = \bar{X}_i'' \bar{X}_i''$  is the variance of the mass fraction of species  $i$ ;  $f_i^\sigma = \bar{\rho} \bar{X}_i'' \bar{X}_i'' \bar{u}_r''$  is the turbulent flux of this variance;  $2f_i \bar{\partial}_r \tilde{X}_i$  is a down-gradient production/destruction; and  $2\bar{X}_i'' \bar{\rho} \bar{X}_i^{\text{nuc}}$  is a variance source/sink due to nuclear burning.

The term  $\mathcal{N}_{\sigma_i}$  represents the dissipation of composition variance due to the numerical scheme, which is discussed further in Section 5.

## 4 RELEVANT TIME-SCALES

The simulations are strongly dynamic, and may be better understood by comparison of several time-scales, which we define here. The convective turnover time-scale is

$$\tau_{\text{conv}} = 2(r_b^c - r_t^c)/v_{\text{rms}}, \quad (13)$$

where  $r_b^c$  and  $r_t^c$  are the radii of the bottom and top convection boundaries, and  $v_{\text{rms}}$  is the rms of the velocity field in the convection zone. The net nuclear (e-folding) burning time-scale for element  $i$  is

$$\tau_{\text{nuc}}^i = \bar{X}_i / \bar{X}_i^{\text{nuc}}. \quad (14)$$

The nuclear (e-folding) burning time-scale due to photo-disintegration of element  $i$  is

$$\tau_{\text{nuc-phot}}^i = 1/\lambda_i, \quad (15)$$

and the nuclear (e-folding) time-scale for burning element  $i$  due to two-body reaction of  $j$  and  $k$  is

$$\tau_{\text{nuc-two}}^i = 1/(\bar{\rho} \lambda_{jk} \bar{Y}_j \bar{Y}_k / \bar{Y}_i), \quad (16)$$

where  $Y_i = X_i/A_i$  are molar abundances of species  $i$ , and  $A_i$  is mean number of nucleons per isotope  $i$ .  $\lambda_i$  and  $\lambda_{jk}$  are nuclear reaction rates expressed as  $N_A \langle \sigma v \rangle$ , where  $N_A$  is Avogadro’s number,  $\sigma$  is the reaction cross-section, and  $v$  the relative velocity of reactants (Clayton 1983; Arnett 1996).

The (e-folding) transport time-scale of element  $i$  is

$$\tau_{\text{tran}}^i = \bar{X}_i / (\nabla_r f_i / \bar{\rho}); \quad (17)$$

and finally, the (e-folding) dissipation time-scale of element  $i$  is

$$\tau_{\text{diss}}^i = \sigma_i / \varepsilon_i, \quad (18)$$

where  $\varepsilon_i$  is the dissipation of variance  $\sigma_i$  which we identify with the residual term  $\mathcal{N}_{\sigma_i}$  defined in equation (12) above and discussed further in Section 5.3.3.

## 5 RESULTS

To initiate convection in our 3D simulation we seed the initial hydrostatic model with small ( $10^{-3}$ ) random perturbations in density and temperature (Meakin & Arnett 2007) in the unstable regions. Convection starts with an increase of turbulent kinetic energy near the base of the convection zone, similar to other qualitatively comparable cases, *e.g.* Mocák et al. (2009), Stancilffe et al. (2011), Woodward, Herwig & Lin (2015). The velocities eventually grow from zero to  $10^{-2}$  of sound speed, to become a self-consistent turbulent cascade, with final amplitudes that happen to be of the same order as MLT velocities because they involve the same buoyancy.

Since the 1D initial model does not contain sufficient dynamic information for self-consistent quasi-static 3D convection, a readjustment occurs as a self-consistent convective flow forms. This is usually referred to as the ‘initial transient’ phase, and is a common feature of 3D stellar hydrodynamics simulations; see Section 5.1. Even with perfect hydrostatic matching of the initial model, a readjustment is required – 3D convection is different from 1D stellar convection theory (e.g. Meakin & Arnett 2007; Arnett et al. 2015).

### 5.1 Initial transients

For neutrino-cooled stages such as oxygen burning, convection is vigorous and turbulent (Meakin & Arnett 2007). One-dimensional (1D) stellar evolutionary sequences use mixing-length theory (MLT), which assumes a specific average correlation between fluctuations in velocity and entropy; these correlations drive the fluxes crucial for thermal balance. In contrast, 3D simulations must develop such correlations in a dynamically self-consistent way, to obtain the appropriate average. This takes a turnover time, after which the turbulent cascade can remove the excess entropy to obtain a balance *on average*. Because mean velocities are dominated by *fluctuations* (Meakin & Arnett 2007), turbulent convection is made up of alternate bursts and pauses, occurring throughout the convection zone. It is intermittent; only the average is quasi-steady. The 1D models cannot provide the dynamically consistent *phases* of the fluctuations which are crucial to accurately determine the net effect of cancellations, and for setting up a consistent 3D initial model.

In 3D stellar interior simulations, this fact, combined with the (generally negligible) errors introduced by mapping a 1D model to a 3D space, leads to an ‘initial transient’ – even if the most exacting hydrostatic balance is enforced in the mean.

### 5.2 Multilayered convective-reactive burning

During the initial transient phase (see Section 5.1 above), the convective plumes emerging from the oxygen burning shell quickly extend into the neon-burning region, which was previously separated by a very narrow region of stability. The two shells merge within the first 100 s ( $\sim 1$  turnover) of the simulated star time. Soon a quasi-steady state is established, when the total turbulent kinetic energy density of the flow in the convection zone reaches roughly  $10^{14}$  erg g $^{-1}$ , at around 300 s ( $\sim 3$  turnovers) of the simulation.

In a local 1D treatment of convection, a linear criterion such as the Ledoux or Schwarzschild defines a region of stability which is capable of preventing mixing, regardless of how weak the stable layer may be. In reality, the ability of a stable layer to survive against turbulent convection depends on both the strength of the stabilizing gradient and the strength of the adjacent turbulence

(the Richardson criterion; Meakin & Arnett 2007; Cristini et al. 2017). In this particular model, the upper convective boundary was calculated by the Ledoux criteria (at a radius around  $7.2 \times 10^8$  cm), and was quickly overwhelmed by the adjacent turbulent flow. The oxygen- and neon-burning shells are rapidly but gently<sup>5</sup> mixed together.

The onset of convection, the subsequent merging of the burning shells, and the establishment of a quasi steady-state, is depicted in Fig. 3 as a group of ‘Kippenhahn plots’, which are space-time diagrams. Shown are the time evolution of (1) the turbulent kinetic energy, (2) mean and variance of  $^{16}\text{O}$  and  $^{20}\text{Ne}$  mass fractions, and (3) nuclear energy generation rates. The top row shows the time evolution of the turbulent kinetic energy (TKE), including, from left to right, the radial, horizontal, and total values. The kinetic energy at a given radius is calculated as half of the variance of the velocity component in the horizontal plane, *e.g.* the radial TKE  $k_r$  is defined by  $2k_r(r) = \sigma_{u_r}^2 = \overline{(u_r - \bar{u}_r)^2}$ . The horizontal TKE is defined by  $2k_h = \sigma_{u_\theta}^2 + \sigma_{u_\phi}^2$ , and the total TKE by  $k_{\text{tot}} = k_r + k_h$ .

The most prominent features of the quasi-steady state include a single convection zone with two internal burning layers, as well as the interplay of turbulent mixing and material entrainment. We describe these features later for  $^{16}\text{O}$  and  $^{20}\text{Ne}$  nuclear burning.<sup>6</sup> The net nuclear burning of other prominent species in the convection zone (*i.e.*  $^{12}\text{C}$  or  $^{28}\text{Si}$ ) are several orders of magnitude smaller and are not discussed further here.

*This novel development is not presently captured in 1D stellar models: a robust current of entrained fuel is delivered from the neon-rich region to the hotter, deeper, oxygen-rich layers, without splitting the convective region.* The process is most clearly seen for  $^{20}\text{Ne}$  which is being drawn into the oxygen-burning shell from the upper boundary. Fig. 4 shows both (*left*) a cross-sectional slice through the 3D simulation; as well as (*right*) the radial profile of the  $\text{Ne}^{20}$  mass fraction in both the initial model and after a quasi-steady state has been achieved. The reason this phenomena has been missed in 1D models is that those models use MLT, which is a local theory, and must be supplemented by ad hoc boundary conditions (Schwarzschild or Ledoux). The correct boundary conditions are nonlinear, dynamic, and complex *i.e.* not linear, static, and simple, as we shall see below.

The nuclear energy production increases in the vicinity of the temperature maximum by a factor of 5. We find a secondary peak in the energy release at  $r \sim 5.7 \times 10^8$  cm, where the main source of nuclear energy is neon burning (equation A2). The contributions to the net nuclear energy generation by different reactions are presented in the left-hand panel of Fig. 5.

In the region of this secondary energy generation peak, the mass fraction of  $^{20}\text{Ne}$  is maintained in a quasi-steady state by a balance between a net inflow from the overlying neon-rich stable layer and depletion by nuclear burning. This balance can be seen by comparing the time-scales for the different processes involved, as shown in the right-hand panel of Fig. 5: the time-scales for destruction of  $^{20}\text{Ne}$  by nuclear burning (blue curve) and inflow by transport (green curve) match in the burning region. In contrast, the overlying layers are dominated by neon transport where its time-scale is

<sup>5</sup>No shocks or even strong pressure waves could be seen, only steady growth of turbulence.

<sup>6</sup>A more comprehensive presentation of the chemical element transport for all the remaining nuclear species in the model is presented in Mocák et al. (2014).

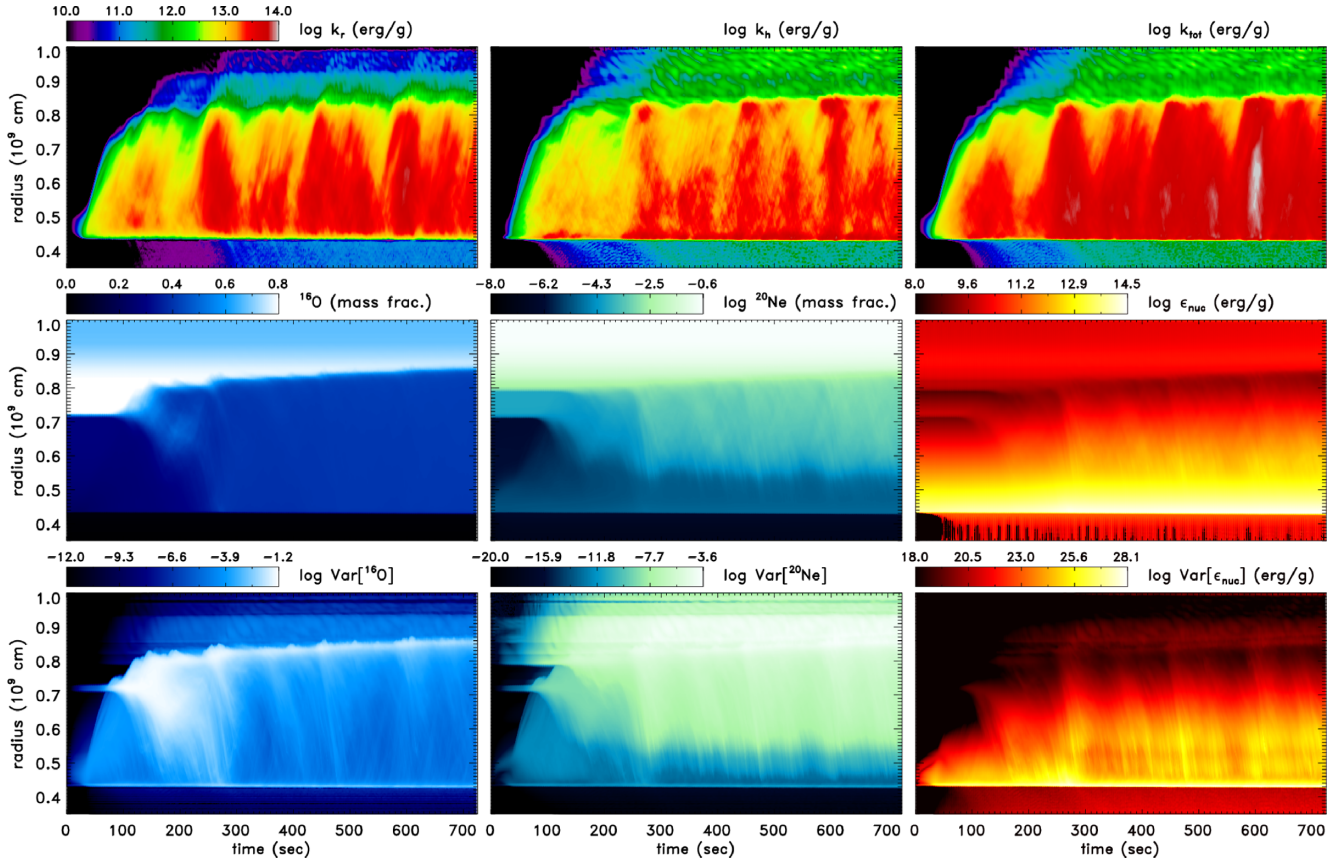


**Figure 3.** Space-time diagrams showing the evolution of various turbulence quantities for model ob . 3d . B. From left to right, the *top row* shows: (left) radial turbulent kinetic energy (TKE); (middle) horizontal TKE; and (right) total TKE. From left to right, the *middle row* shows: (left) mean  $^{16}\text{O}$  abundance; (middle) base-10 logarithm of mean  $^{20}\text{Ne}$  abundance; (right) mean net-nuclear energy generation rate. The *bottom row* shows, from left to right: (left) base-10 logarithm of  $^{16}\text{O}$  abundance variance; (middle) base-10 logarithm of  $^{20}\text{Ne}$  abundance variance; and (right) base-10 logarithm of net-nuclear energy generation variance.

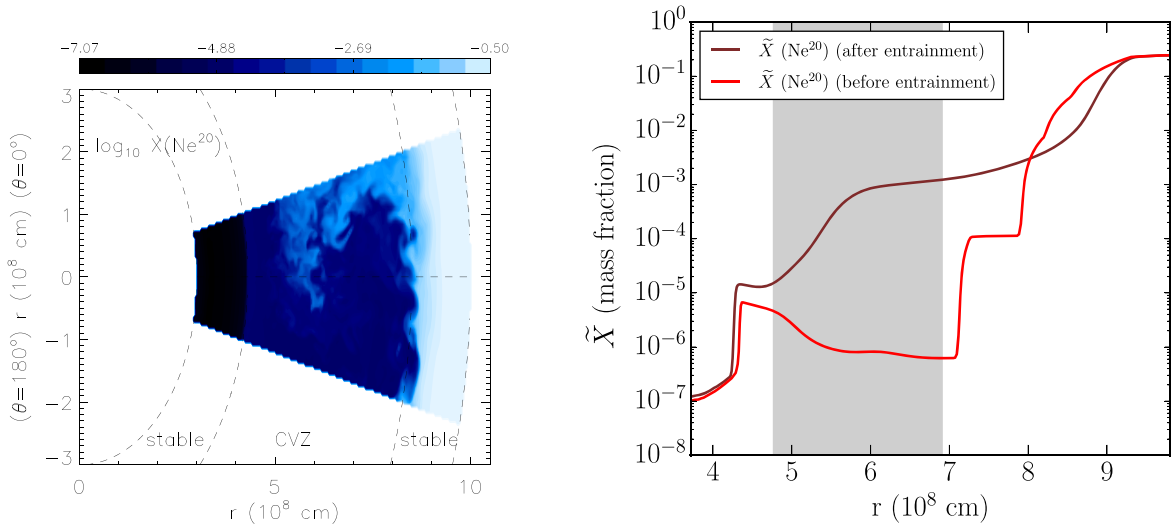


**Figure 4.** Left: Snapshot of  $\log_{10} X^{(20)\text{Ne}}$  in a meridional plane, where the inner dashed lines mark boundaries between convectively stable layers and convection zone (CVZ), and the outer dashed lines mark the edges of the computational domain. Right: Profiles of  $^{20}\text{Ne}$  mass fraction before (red) and after (brown) the entrainment event. The shaded vertical region highlights the area of significant nuclear changes in the  $^{20}\text{Ne}$  abundance, where its absolute rate of change due to nuclear burning  $|\tilde{X}_{ne20}^{nuc}|$  exceeds 2 per cent of its maximum value.

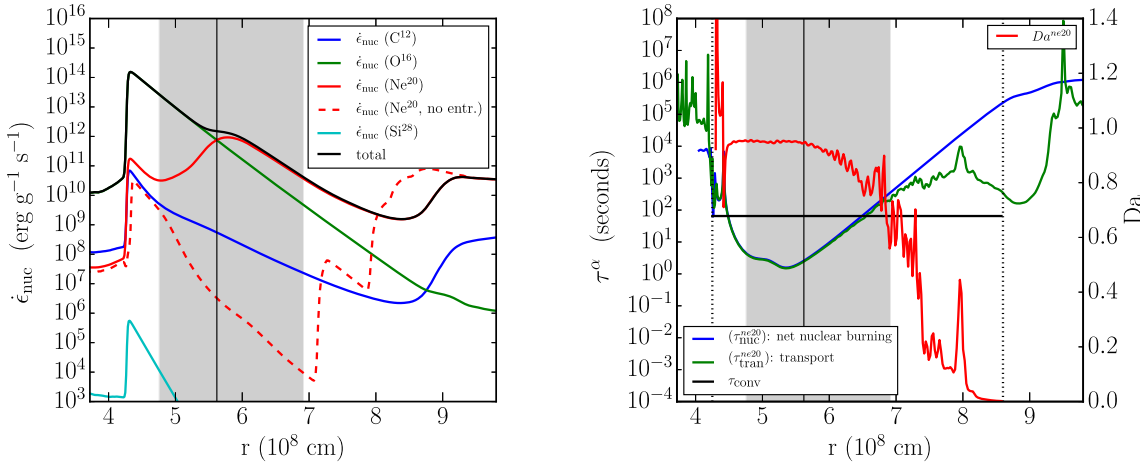


**Figure 5.** Left: Nuclear energy production rates due to burning of  $^{12}\text{C}$ ,  $^{16}\text{O}$ ,  $^{20}\text{Ne}$ , and  $^{28}\text{Si}$ , using the diagnostic approximations in Appendix A. The vertical solid line marks the maximum rate of change of neon density due to nuclear burning, at around  $5.6 \times 10^8 \text{ cm}$ . The shaded vertical region highlights the area as described in Fig. 4. The dashed line represents nuclear production rate due to  $^{20}\text{Ne}$  burning prior the entrainment event. Right: Damköhler number  $Da$  and the transport and net nuclear-burning time-scales  $\tau$  for  $^{20}\text{Ne}$  as defined by equation (14), equation (17), and equation (19). The two vertical dotted lines mark convection zone boundaries. All curves are derived from mean fields calculated for central time at 1060 s of the simulation.

$\sim 3$  orders of magnitude shorter than that for depletion by nuclear burning.

A Damköhler number,  $Da$ , may be defined as the ratio of transport to nuclear burning time-scales. Since we have more than one burning process, multiple Damköhler numbers should be defined, one for each reaction process  $i$ :

$$Da^i = \tau_{\text{tran}}^i / \tau_{\text{nuc}}^i. \quad (19)$$

For  $Da \sim 1$ , such that the transport time-scale is comparable to the burning time-scale, we have the regime of convective-reactive mixing (Herwig et al. 2011). In this regime, it is important to model the convection well, in order to predict the coupled mixing and burning correctly. Such convective-reactive situations are likely to be common in stellar evolution – if allowed by the evolutionary algorithm. They might be common, for instance, in the early Universe in low-metallicity stars (Fujimoto, Ikeda & Iben 2000; Schlattl et al. 2002), or during dredge-up in AGB stars (Goriely & Siess 2004; Herwig 2004).

The Damköhler number varies across a convective region because of the local variation in transport and nuclear time-scales. The nuclear time-scale depends on burning rates which vary with fuel abundance, density, and temperature, while the transport time-scale is determined by the topology of the velocity field. In the upper layers of the convection zone in our simulation, the transport time-scale is much shorter than the nuclear burning time-scales, so  $Da^{ne20} \ll 1$ . There is much more neon entrained and transported than nuclear burning is able to destroy. These time-scales become close only at around  $7 \times 10^8 \text{ cm}$ , where effective nuclear destruction of entrained  $^{20}\text{Ne}$  begins (see right-hand panel of Fig. 5).

It is instructive to compare this 3D result to 1D simulations of similar convective-reactive events. One such class of calculations is the ingestion of protons into He-burning convective regions ('proton ingestion episodes'). These calculations result in a splitting of the He convection zone into two parts (see e.g. Herwig et al. 1999; Campbell & Lattanzio 2008). The split occurs because the large energy release from hydrogen burning creates a temperature inversion at the point of peak H-burning luminosity, creating a (formally) stable region just below. If time-dependent mixing is used in the

1D calculation, this peak occurs at the point where the lifetime of a proton against capture by  $^{12}\text{C}$  is just equal to the time-scale of convective mixing, i.e.  $Da = 1$ . In some studies it is explicitly enforced that the hydrogen is mixed down to the point where  $Da = 1$  (e.g. Fujimoto et al. 2000).

In contrast, our 3D calculation shows that, in the neon ingestion case, the  $Da \sim 1$  condition defines a substantial burning region – rather than a single radial location. This suggests that a split of the convective zone is less likely, as the burning is distributed rather than sharply peaked. Such splitting<sup>7</sup> is likely to be an artefact of the 1D formulation. In order for a radial velocity to go to zero in a quasi-steady state, baryon conservation requires a finite horizontal velocity (Arnett et al. 2015), which in turn implies a shear instability and probably mixing instead of splitting. This may be considered a boundary issue, or 'overshooting'.

The (smooth) peak of nuclear energy release from neon burning is actually located near the middle of the burning region, at around  $5.7 \times 10^8 \text{ cm}$  (Fig. 5). Neon mixes down still further, to  $5 \times 10^8 \text{ cm}$ . As suggested by Herwig et al. (2011), the width of these regions must be due to a combination of factors, such as the temperature sensitivity of the particular nuclear reactions, the range of plume velocities, and the various mixing ratios in the plumes of (in our case) neon-enriched material. In summary, the 3D simulations show that the 1D treatments of convective-reactive events miss some crucial elements that could significantly change these phases.

Our 3D results are qualitatively different from our 1D results for the same initial model, which we regard as a limitation in the 1D formulation. At present 1D stellar evolution is apparently incomplete in its ability to represent spherically averaged 3D effects. The 1D stellar evolutionary sequence does not show a Ne–O shell merger, even at later times, and shows a failure just like the 1D results for 'splitting convection regions' mentioned above. While

<sup>7</sup>In the case of the star we have simulated, a splitting in 1D would be expected at a radius of  $\sim 6.5 \times 10^8 \text{ cm}$ . This is the location where  $\tau_{\text{conv}} = \tau_{\text{nuc}}$ , i.e. the intersection of the blue and black lines in the right-hand panel of Fig. 5. This is well above the location of the main burning in the 3D simulation (vertical line in Fig. 5).

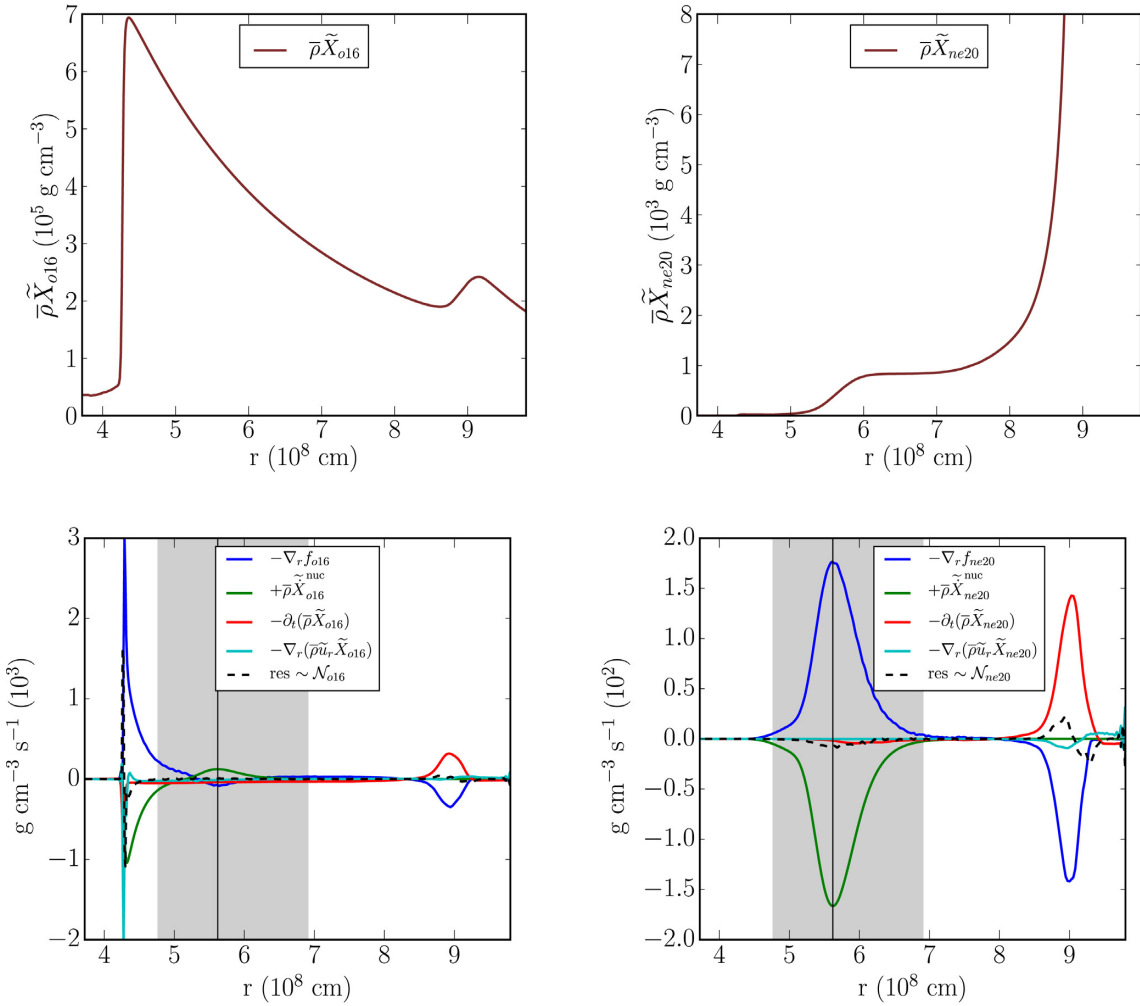


**Figure 6.** Top: Profiles of  $^{16}\text{O}$  and  $^{20}\text{Ne}$  density mean fields. Bottom:  $^{16}\text{O}$  and  $^{20}\text{Ne}$  density transport equations. The shaded vertical region and vertical line as defined in Fig. 5.

there is some neon present in the O-burning convection zone of the 1D model (Fig. 1), its nuclear energy production rate is negligible, being  $\sim 6$  orders of magnitude lower than that of oxygen (see bottom panel of Fig. 5; dashed-red curve). In contrast, the 3D model shows that the energy release from Ne burning dominates that of O in the top half of the convection zone.

Regardless of whatever the final answer may be for the evolution of Ne- and O-burning shells, the inconsistency of 1D and 3D models is a cause to question present in 1D evolutionary scenarios.

### 5.3 Mean-field analysis of 3D simulation data

We use the three composition-related mean-field RA-ILES equations to interpret our 3D simulation data, which we depict graphically in Figs 6–8. Each of these balance equations is discussed in the following subsection in turn, with a focus on a physical interpretation of each term in the equations.

#### 5.3.1 Mean composition

The mean profiles of  $^{16}\text{O}$  and  $^{20}\text{Ne}$  mass fraction are presented in the top row of Fig. 6; while the bottom row of the same figure shows the individual terms in the mean-field balance equation given

by equation (6) which underly these profiles. This figure shows that the composition profiles  $\bar{\rho}\tilde{X}_i$  are established as an interplay between the material entrainment, turbulent mixing, and nuclear burning.

**Time dependence:**  $\bar{\rho}\tilde{D}_t\tilde{X}_i = \partial_t(\bar{\rho}\tilde{X}_i) + \nabla_r(\bar{\rho}\tilde{X}_i\tilde{u}_r)$ . While the convective layer is in a quasi-steady state, ongoing mixing at the upper boundary increases the depth of the convection zone over time. The signature of this mass entrainment appears in the Eulerian component of the time derivative, which is plotted as the red curve in Fig. 6. By contrast, the change in the composition profile due to an overall expansion or contraction is negligible, as revealed by the turquoise curve.

**Turbulent transport:**  $-\nabla_r f_i = -\nabla_r(\widetilde{\bar{\rho}u''_r X''_i})$ . The stable layer material which is mixed into the convective layer is transported by turbulent velocity fluctuations. This spatial redistribution of material is shown by the blue curve in Fig. 6 where we see that  $^{16}\text{O}$  and  $^{20}\text{Ne}$  are transported out of the boundary layer ( $r \sim 9 \times 10^8 \text{ cm}$ ) and into the lower nuclear burning regions of the convection zone ( $r < 7 \times 10^8 \text{ cm}$ ). A simple balance is found: the transport out of the stable layer is closely matched by the time rate of change there; and at the other end, the rate at which material is being brought into the nuclear burning zone is balanced by the rate it is being destroyed by nuclear reactions.

In the case of  $^{20}\text{Ne}$ , the turbulent transport at the outer convective boundary shows depletion by downdrafts – there is more  $^{20}\text{Ne}$  going out from the region than is going in. In contrast, the transport is positive in the neon-burning region below. This indicates that there is more neon going into this region than out, and the net input is equal to the  $^{20}\text{Ne}$  burned by nuclear reactions. The situation is almost identical for  $^{16}\text{O}$ , except there is additional transport of freshly produced oxygen in the neon-burning layer due to its photodisintegration at  $r \sim 5.7 \times 10^8 \text{ cm}$ .

**Nuclear burning:**  $\bar{\rho} \tilde{X}_i^{\text{nuc}}$ . The rate at which the mean abundance of  $^{20}\text{Ne}$  is changed due to nuclear burning is shown by the green curve in Fig. 6. It reveals a region of depletion near the lower part of the convection zone where the temperature and densities rise above  $\sim 1.9 \times 10^9 \text{ K}$  and  $\sim 7 \times 10^5 \text{ g cm}^{-3}$ , respectively. The  $^{20}\text{Ne}$  burning rate is governed by the rate at which entrained material is transported into the burning region.

The width of the neon-burning region is set at the upper end by the reaction rates which are a function of the density and temperature, so that burning does not begin until the material is transported below a radius of  $7 \times 10^8 \text{ cm}$ . At lower radii, the burning region is truncated by the complete depletion of the  $^{20}\text{Ne}$  as it is being transported downwards. The nearly symmetrical, gaussian shape is therefore a coincidence of the near balance in time-scales between these two competing processes: a more vigorous turbulent transport, and hence a shorter convective mixing time-scale through the burning region, would result in a deeper lower boundary consisting of fuel which was able to penetrate deeper before being completely consumed. The higher temperatures present near the base of the oxygen-burning shell, however, ensures that the bulk of any entrained  $^{20}\text{Ne}$  is consumed before traversing the entire convective layer, resulting in a structure with ‘stacked’ nuclear-burning zones and a stratified composition. The plateau in  $\bar{\rho} \tilde{X}_{\text{ne}20}$ , at  $r \sim 6.5 \times 10^8 \text{ cm}$  (see Fig. 6), reflects this balance between entrainment and burning.

The transport of  $^{16}\text{O}$  in the upper layers of the convection zone shows similar properties to that of  $^{20}\text{Ne}$ , with oxygen being pulled down into the convection zone from the upper stable layer by turbulent velocity fluctuations. However, in layers where Ne burning dominates,  $^{16}\text{O}$  is produced through photo-disintegration:  $^{20}\text{Ne}(\gamma, ^{16}\text{O})^{24}\text{Mg}$  (see lower left-hand panel in Fig. 6). Towards smaller radii, oxygen depletion continues to increase due to nuclear fusion.

**Numerical residual:**  $\mathcal{N}_i$ . Unlike traditional solvers of the Navier–Stokes equations, a conservative hydrodynamics algorithm such as PPM results in errors in conservation laws with magnitudes comparable to machine precision. Therefore, the residuals found in the balance equations are due to the much larger effects – and can be understood as loss of information at the grid level (dissipation and diffusion).

A quantitative measure of this numerical residual is shown by the dashed black curve in Fig. 6. The impact that it has on the mean flow can be quantified by comparing the amplitude of this curve with the other dominant physical processes controlling the time evolution. In comparison to nuclear-burning and turbulent transport, which are the dominant processes, the numerical flux is relatively small over the majority of the domain. However, it does make an important contribution in narrow regions around both the upper and lower convective boundaries (Fig. 6). Here, turbulent boundary layers develop (Landau & Lifshitz 1959, section 44). As expected, this flux is present exactly where the mean composition fields possess steep gradients. The steady presence of internal wave fields in and

around the convective boundaries ensures that the material fields are constantly in motion against the computational mesh, thereby weakening the gradients. The strength of this numerical flux is seen to diminish with finer resolution as gradients are better resolved (Arnett et al. 2015; Cristini et al. 2017).

### 5.3.2 Turbulent composition flux

The turbulent composition flux  $f_i$  represents the rate at which matter of species  $i$  is transported across a given spherical shell. Flux profiles and balance equation terms for the flux evolution equations for  $^{16}\text{O}$  and  $^{20}\text{Ne}$  are presented in Fig. 7. The negative values of the fluxes indicate that they are oriented towards the stellar centre, which is consistent with the picture of entrainment from upper stable layers dominating the mixing of new material into the convection zone.

**Time dependence:**  $\bar{\rho} \tilde{D}_t(f_i/\bar{\rho}) = \partial_t(f_i) + \nabla_r(f_i \tilde{u}_r)$ .

The rate of change of the flux, at a given spatial location and within a fixed mass shell (i.e. at a fixed Lagrangian coordinate) – shown by the orange and brown curves in Fig. 7 – is found to be small compared to the other terms determining the flux profile, indicating a quasi-steady balance. The expansion velocities in the model are only  $\sim 10^2 \text{ cm s}^{-1}$ , which is 5 orders of magnitude smaller than the rms of the turbulent velocity field ( $\sim 10^7 \text{ cm s}^{-1}$ ). The quasi-steady flux of  $^{16}\text{O}$  and  $^{20}\text{Ne}$  is here due to a balance between nuclear burning, turbulent transport, and pressure-force, and centrifugal-force coupling.

**Turbulent production:**  $-\tilde{R}_{rr} \partial_r \tilde{X}_i$ . The presence of radial velocity fluctuations in regions where there is a mean radial composition gradient leads to the production of a turbulent mass flux. This process involves the radial component of the turbulent kinetic energy  $k_r = \tilde{R}_{rr}/2$  and the mean composition gradient for isotope  $i$ , given by  $\partial_r \tilde{X}_i$ . In the case of  $^{20}\text{Ne}$ , where the mean abundance gradient is everywhere positive, the presence of turbulent velocity fluctuations leads to a *downward directed* mass flux, and hence has a *negative sign*. This term is shown by the red curve in Fig. 7. The situation is similar for  $^{16}\text{O}$  with the exception of (1) the neon-burning region – where the oxygen abundance locally increases due to photo-disintegration of neon – giving rise to a contribution to the outward-directed composition flux; and (2) the region around the lower boundary, where oxygen burning produces a very steep gradient and hence a large contribution to the downward-directed flux component.

**Pressure-force coupling:**  $-\left(\overline{X''_i \partial_r \bar{p}} + \overline{X''_i \partial_r p'}\right)$ . This process is localized near the upper and lower convective boundaries where it peaks and drops off on either side of the interface. These terms are shown by the turquoise coloured curve in Fig. 7. On the convection zone side of each boundary, the overall strength of this effect drops as the buoyancy diminishes relative to the velocity fluctuations; on the stable side of each boundary, the strength of buoyancy is set by the entropy stratification while the turbulent velocity fluctuations decay with distance from the boundary.

Material which resides in the stable layer is buoyant relative to material in the adjacent convection zones by virtue of its relative mean molecular weight and entropy: in the upper stable layer, the material is lighter per ion and is in a higher entropy configuration. Therefore, as material is drawn down into the convection zone by turbulent velocity fluctuations its downward motion is resisted by this buoyancy. As the freshly entrained stable layer material is dredged deeper into the convection zone, it is continually being mixed with its surroundings by turbulence which reduces its relative buoyancy. By the time this newly ingested material reaches the far

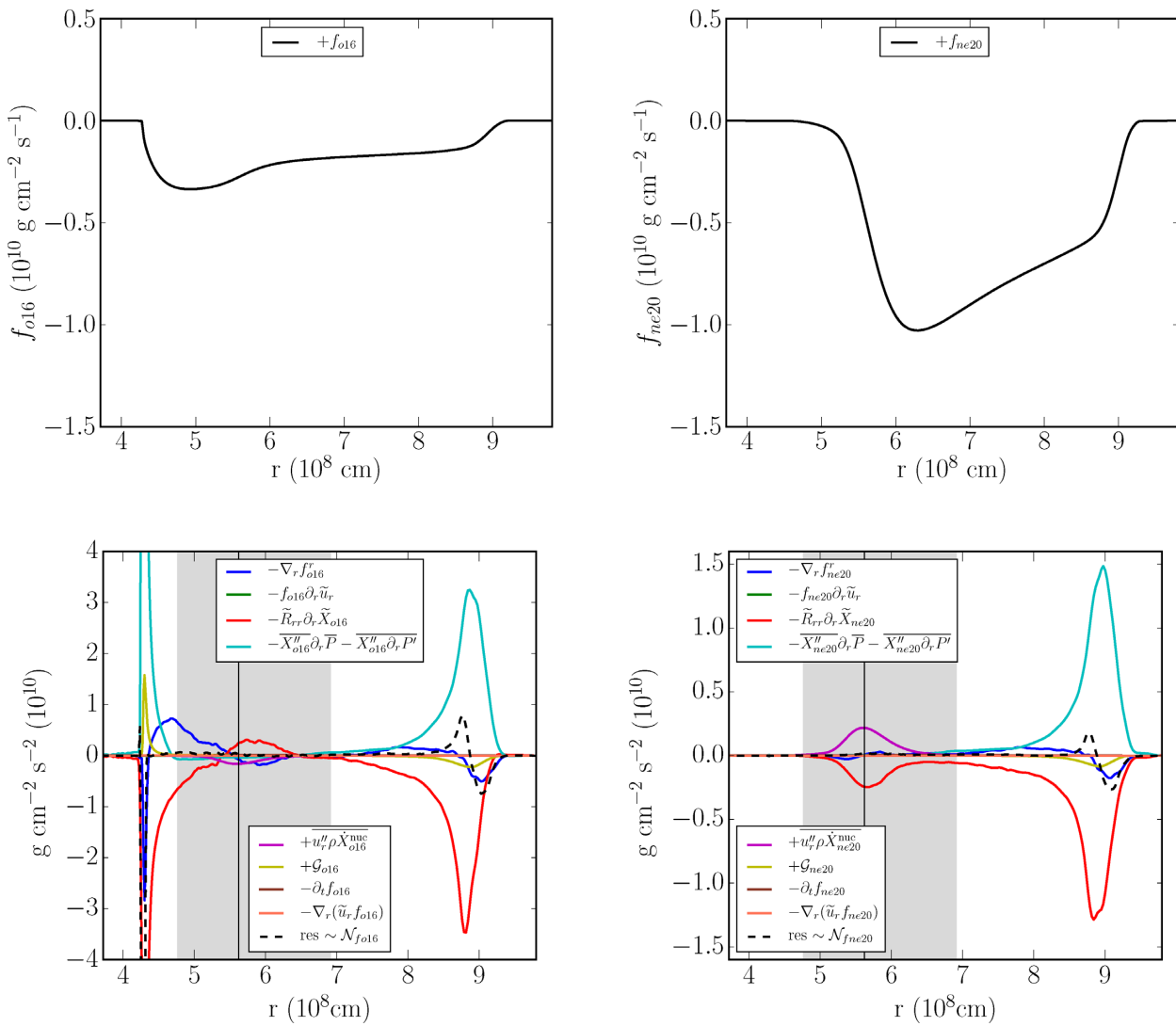


**Figure 7.** Top: Profiles  $^{16}\text{O}$  and  $^{20}\text{Ne}$  turbulent flux mean fields. Bottom:  $^{16}\text{O}$  and  $^{20}\text{Ne}$  turbulent flux mean fields transport equations. The shaded vertical region and vertical line as defined in Fig. 5.

end of the convection zone the relative buoyancy affecting its flux is negligible.

The part of this term that reads  $-\overline{X_i''} \partial_r \bar{p}$  can be rewritten to highlight its relationship to buoyancy: using the identity  $\overline{X_i''} = -\overline{\rho X_i'}/\overline{\rho}$  and hydrostatic equilibrium  $\partial_r \bar{p} = -\overline{\rho g}$  we find

$$-\overline{X_i''} \partial_r \bar{p} = \overline{X_i' \rho' \tilde{g}}. \quad (20)$$

The term  $-\overline{X_i''} \partial_r p'$  is related to pressure fluctuations and is of a dynamic rather than a thermodynamic origin. In the anelastic approximation, the pressure fluctuations are governed by a Poisson equation

$$\Delta p' = -\nabla : (\rho_0 \vec{u}' \oplus \vec{u}') - \nabla \cdot (\rho' \vec{g}). \quad (21)$$

In stably stratified layers the buoyancy component dominates; in the well-mixed turbulent layer the advective term dominates (Viallet et al. 2013); and the partially mixed boundary layer is a region of transition between the two.

**Centrifugal-force coupling:**  $\mathcal{G}_i$ . This term is driven by horizontal flow produced by the deflection of plumes at the inner boundaries of the convection zones and provides a radially directed acceleration to the matter with which it is coupled. At the upper boundary, the

plumes which ultimately become horizontal flows carry material which is primarily representative of the mean composition of the convection zones, and hence will be depleted in those isotopes which are being actively entrained at the upper boundary. Therefore, the net effect of this process will be a net *negative* contribution to the entrained mass flux. Since we are considering downward directed fluxes of material being entrained at the upper boundary, this term will therefore act as a *source* for this entrained matter flux. This term is plotted as the yellow curve in Fig. 7.

A similar, but mirrored effect, takes place at the lower boundary for  $^{16}\text{O}$ .

**Nuclear burning:**  $u_r'' \rho \dot{X}_i$ . As the  $^{20}\text{Ne}$  approaches the bottom of the convection zone it begins to undergo nuclear burning which diminishes fluctuations in its abundance, and therefore reduces the downward-directed mass flux. This process is represented by the magenta curve in Fig. 7 where it can be seen to operate in the neon-burning region. This same process also operates for the  $^{16}\text{O}$  flux, but with the opposite sign.

**Turbulent transport:**  $-\nabla_r f_i^r = -\nabla_r \left( \widetilde{\rho u_r'' u_r'' X_i'} \right)$ . In the same manner in which velocity fluctuations act to redistribute Reynolds stress, or its trace, the turbulent kinetic energy  $k = \text{Tr}(\widetilde{\rho u_i'' u_j''})$ ;

velocity fluctuations also redistribute compositional flux ( $f_i = \widetilde{\rho u'' X_i''}$ ) in space. Although not a dominant effect in controlling the radial profile of  $^{20}\text{Ne}$  flux, it does transport some of the downwardly directed flux from the middle of the convection zone to the upper stable layer and the region just below the  $^{20}\text{Ne}$ -burning zone. This spatial redistribution can be seen in Fig. 7 where it is represented by the darker blue curve.

**Numerical residual:**  $\mathcal{N}_{f_i}$ . The implicit action of turbulent cascade on the turbulent composition fluxes is apparent at the convective boundaries.

### 5.3.3 Composition variance and its dissipation rate

Composition variance  $\sigma_i$  is a measure of the amplitudes of the composition fluctuations at a given radial location in the stellar interior. It is typically largest at convective boundaries (where the gradients are steepest), due to the oscillatory distortion of the boundary by gravity waves as well as the presence of turbulent entrainment of material into the convection zone. This  $\sigma_i$  and the terms in the balance equation for this mean-field variable is shown in Fig. 8. The  $^{16}\text{O}$  variance distribution shows maximum values at both convective boundaries, whereas  $^{20}\text{Ne}$  peaks only at the upper boundary due to a lack of neon at deeper layers due to depletion by nuclear burning and turbulent mixing.

Dissipation is an important feature of turbulence. In the ILES approach, the Euler equations are solved so that dissipation is implicitly included; in our case, the numerical algorithm provides an effective damping at the dissipation (sub-grid) scale. The rate at which composition fluctuations are destroyed by this process can be expressed by a dissipation time-scale, as in equation (18). We associate this time-scale with the residual of the transport equation of variance (equation 12) since it characterizes the magnitude of numerical dissipation. We discuss this important feature further in the paragraph below, under the subheading *Numerical Residual*.

**Time dependence:**  $\widetilde{\rho D}_t \sigma_i = \partial_t(\bar{\rho} \sigma_i) + \nabla_r(\widetilde{\rho u_r} \sigma_i)$ . The variance is in a steady state throughout most of the computational domain but does show a sign of the convective boundary mixing at the upper boundary. The signature of this mass entrainment appears in the Eulerian time derivative which is shown by the turquoise curve in Fig. 8 – while the overall effect of background expansion on the mean variance field is negligible, as shown by the magenta curve.

The sine wave-like shape of the time dependence is due to the outward migration of the variance peak following the mass entrainment (note the sign of the terms plotted as indicated in the figure legend).

**Turbulent production:**  $-2f_i \partial_t \widetilde{X}_i$ . The primary source of variance in the composition field is turbulent production, which is analogous to the source of turbulent flux discussed above. In this case, variance is produced when a turbulent mass flux is present in regions where there is a mean composition gradient. Physically, the growth of variance can be thought of as the coupling of the composition fluctuation associated with the turbulent flux to the newly created composition fluctuation which is generated by the associated velocity fluctuation.

In the case of the  $^{20}\text{Ne}$ , the net downward-directed composition flux works against a positive gradient in the  $^{20}\text{Ne}$  abundance (see Fig. 4), thus amplifying the local fluctuations and resulting in an overall positive increase in the mean variance. Production is seen to dominate in and around the upper boundary, then drops off with depth into the convection zone, until a small peak in the

$^{20}\text{Ne}$ -burning region where again the mean composition gradients are very steep – in this case due to the nuclear depletion of  $^{20}\text{Ne}$ . This term is shown by the green curve in Fig. 8. The situation for  $^{16}\text{O}$  is similar, but has significant contributions at both boundaries.

**Turbulent transport:**  $-\nabla_r f_i^\sigma = -\nabla_r (\widetilde{\rho u'' X_i'' X_i''})$ . Variance is transported by the variance flux  $f_i^\sigma$  which is the correlation of a velocity fluctuation with the square of the composition fluctuation. As with all turbulent transport, it is a conservative process and neither creates nor destroys variance but simply redistributes it spatially. The redistribution of  $^{20}\text{Ne}$  has a relatively simple behaviour in our 3D models: the variance that is generated within the upper boundary by turbulent production is moved both outward, to a region lying just above the main region of turbulent production; as well as being moved downward to the bottom of the  $^{20}\text{Ne}$ -burning region to the depth at which  $^{20}\text{Ne}$  is completely consumed by nuclear burning. The case for  $^{16}\text{O}$  is similar, but can be seen operating at the lower convective boundary as well.

**Nuclear burning:**  $2X_i'' \rho \dot{X}_i^{\text{nuc}}$ . Nuclear burning results in the growth or decay of fluctuations due to nuclear reactions. In the case of  $^{20}\text{Ne}$ , the abundance is depleted through nuclear burning and so this term acts as a sink for the variance that was transported or produced in the  $^{20}\text{Ne}$ -burning zone.

**Numerical residual (dissipation):**  $\mathcal{N}_{\sigma_i}$ . The dashed black curve in Fig. 8 shows the residual term. The thin solid black curves shows a model of the scalar dissipation which assumes that the dissipation time-scale is equal to the Kolmogorov damping time-scale, defined by

$$\tau_L \equiv \left( \frac{\nu}{\epsilon} \right)^{1/2} \equiv \frac{\tilde{k}}{\epsilon_k}, \quad (22)$$

where  $\nu$  is viscosity,  $\epsilon$  is the turbulent kinetic energy transfer rate, and  $\tilde{k} = 1/2 \widetilde{u_i'' u_i''}$  is the Favrian-specific turbulent kinetic energy mentioned also in Section 5.2. Here,  $\epsilon_k$  is the dissipation rate of  $k$ , which can be approximated by  $\epsilon_k \sim u_{\text{rms}}^3 / L$ , where  $L$  is the scale of the flow *i.e.* essentially the size of convection zone (Arnett, Meakin & Young 2009; Cristini et al. 2017).

These time-scales allow us to test if our simulation results agree with Kolmogorov's first similarity hypothesis, which states that in turbulent flows with high Reynolds numbers, the statistics of the motion at the dissipation scale has a universal form that is uniquely determined by  $\nu$  and  $\epsilon$  (Pope 2000). We do indeed find that the scalar dissipation rates in our simulation, calculated using  $\tau_L$  as defined above, provides a good fit to our data (Fig. 8), with

$$\mathcal{N}_{\sigma_i} \sim \frac{\bar{\rho} \sigma_i}{\tau_L} \sim \bar{\rho} \sigma_i \frac{\epsilon_k}{\tilde{k}} \sim \bar{\rho} \sigma_i \frac{1}{L} \frac{u_{\text{rms}}^3}{\tilde{k}}. \quad (23)$$

This result supports the physical consistency of the sub-grid scale numerics of our simulation and the ILES approach, even at rather low spatial resolution and effective Reynolds numbers,  $\text{Re}^{\text{eff}}$ . In our simulation,  $\text{Re}^{\text{eff}} \sim N_c^{4/3} \sim 1440$ , where  $N_c \sim 234$  is the number of radial grid points across the convection zone. That the composition variance dissipation rate  $\mathcal{N}_{\sigma_i}$  is directly proportional to  $\bar{\rho} \sigma_i / \tau_L$  (equation 23) is consistent with mixing models of molecular diffusion. This further confirms the assumption that the rate of scalar mixing is determined by scalar variance production at large scales (Fox 1995).

Despite the inviscid assumption of the Euler equations, scalar dissipation in the composition variance will occur because of the presence of a numerical mass flux  $\mathcal{Y}$ . This will modify all continuity equations such that they have a form:

$$\partial_t(\rho X_i) = \nabla \cdot (\rho u_i X_i + \mathcal{Y}) + \rho \dot{X}_i^{\text{nuc}}. \quad (24)$$

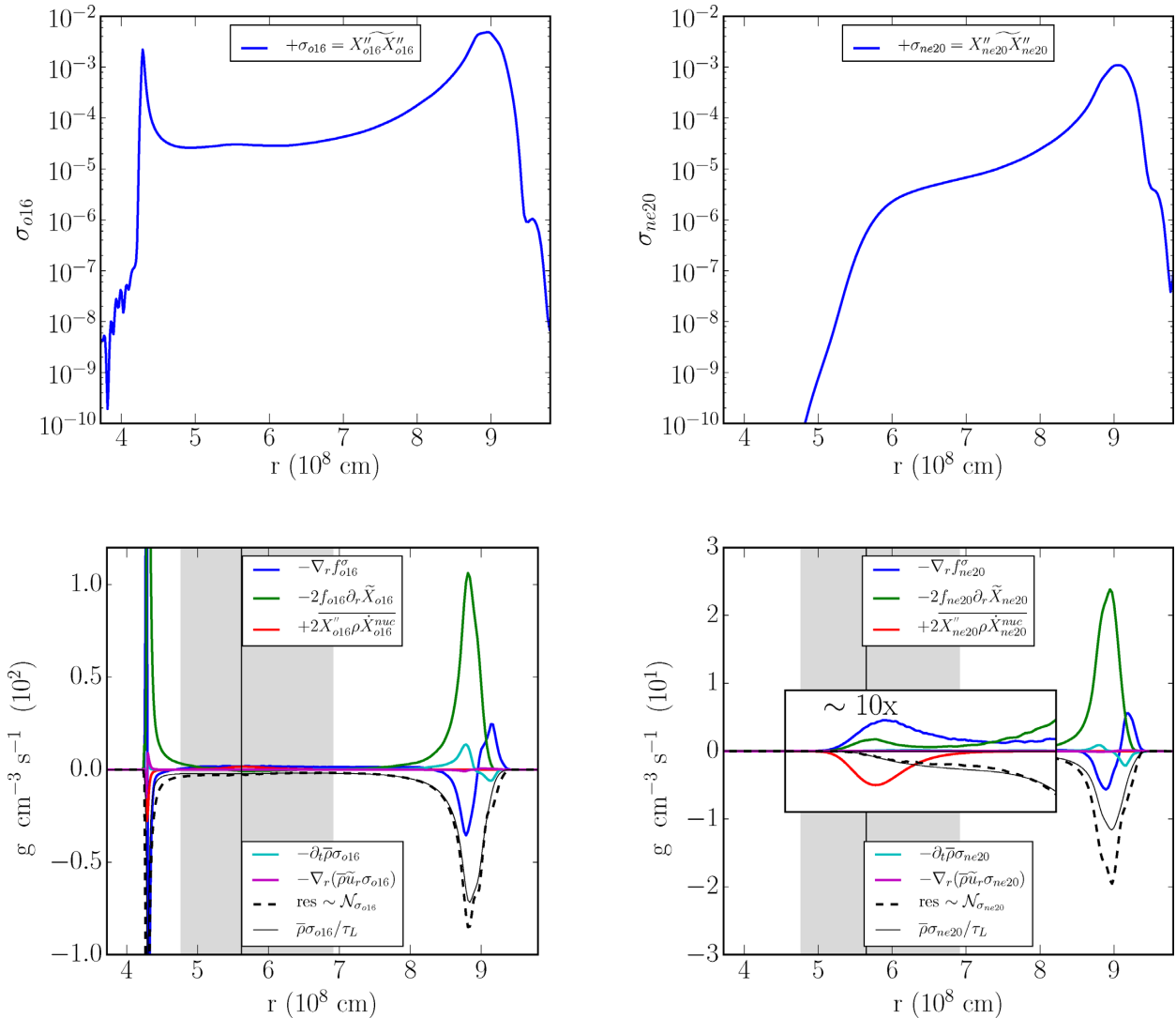


**Figure 8.** Top: Profiles of  $^{16}\text{O}$  and  $^{20}\text{Ne}$  variances. Bottom:  $^{16}\text{O}$  and  $^{20}\text{Ne}$  variance transport equations. The shaded vertical region and vertical line as defined in Fig. 5.

In these equations  $\nabla \cdot \mathcal{Y}$  is therefore a conservative redistribution term that will lead to smearing effects, i.e. numerical diffusion. Mass conservation is however still maintained across the domain. We use these equations to represent the modified equations being solved by the numerical algorithm.

#### 5.4 Effects of resolution

As mentioned above, the effective Reynolds number of the flow in our simulation is  $\text{Re}^{\text{eff}} \sim 1440$  and it is thus expected to be in the turbulent regime. This is supported by our finding that the variance dissipation is proportional to the variance over the large eddy time-scale – a phenomenology expected when turbulence is developed and has an inertial range.

Our previous work utilizing RA-ILES ('RANS') analysis shows that the qualitative analysis of the *interior* of convection zones is not strongly affected by resolution, for a wide range of effective Reynolds numbers ( $\text{Re}^{\text{eff}} \sim 500\text{--}3300$ ; Viallet et al. 2013; Mocák et al. 2014; Cristini et al. 2017). This shows that our

RA-ILES technique is useful even at relatively low resolution – at least for PPM hydrodynamics. Moreover, the RA-ILES approach can be used to assess resolution dependence and convergence by analysing the residuals defined in by the mean-field equations.

The boundaries of convection zones, on the other hand, are generally underresolved in stellar interior simulations. This is readily identifiable – and quantified – in the RA-ILES residuals (eg.  $\mathcal{N}$  in Figs 6 and 7). In the current simulation, the lower boundary has a large 'spike' in residuals. This is a turbulent boundary layer, and is relatively thin, with steep gradients in various quantities. We have previously shown that these residual spikes diminish with increasing resolution (Cristini et al. 2017). The top boundary also shows a spike in the residuals, but is much less pronounced because of the shallower gradients present there – it is a 'softer' boundary.

While these residuals must affect the quantitative rate of entrainment, we do not expect the qualitative features of the convective-reactive flow to be strongly impacted, especially since the residuals become negligible away from the convective boundaries.

## 6 SUMMARY

We have analysed coupled turbulence and nuclear burning in a 3D hydrodynamic implicit large eddy simulation (ILES) of an oxygen-burning shell in the core of a  $23 M_{\odot}$  supernova progenitor star.

### 6.1 Hydrodynamic simulation

Our initial stellar structure encompassed a single oxygen-burning convection zone with a stable Ne-burning layer above. After an initial transient episode which led to a gentle merging of the O-burning convective shell with the Ne-burning shell, a quasi-steady layered-shell state was formed. Two layers of stable nuclear burning were set-up in the joined velocity field of a single convection zone, with  $^{16}\text{O}$  dominating the nuclear energy production at the bottom of the convection zone, but  $^{20}\text{Ne}$  dominating in the upper layers.

The quasi-static state showed a Ne-burning rate in the convection zone up to seven orders of magnitude higher than in the initial 1D model. This was due to a steady entrainment of  $^{20}\text{Ne}$  into the hotter, oxygen-burning shell.

Further, neon burning was found to occur over a wide region in the convection zone. This is in contrast to the situation found in 1D codes for similar convective-reactive cases, for example during proton ingestion into He-burning regions in low-mass stars. As a consequence of limitations in their mixing algorithms, 1D codes generally show burning in a very thin layer, at a depth where the ratio of the burning time-scale equals that of the convective turnover time-scale, i.e. where the Damköhler number equals one. In our simulation this defines only the top of a wider burning region, and the peak of the burning is well below this point (Fig. 5).

### 6.2 RA-ILES analysis

The key results presented in this paper are based on a RA-ILES analysis of the composition-related mean fields found for our 3D ILES simulation data, and extend our previous investigations which used the turbulent kinetic energy (TKE) equation.

We develop RA-ILES equations (Section 3) which describe the time evolution of mean composition, turbulent composition flux, and composition variance for each isotope present in the stellar plasma. The equations derived are exact and do not employ approximations to the extent that the continuum approximation is appropriate and flow features are resolved. This contrasts with use of closure relationships and truncations of the RANS equations to construct models of turbulence. The RANS equations, when closed by 3D ILES numerical simulations (RA-ILES), are able to represent the full range of hydrodynamical behaviour that is present in a stellar interior simulation.

Our detailed RA-ILES analysis revealed, over the time-scale of the simulation ( $\sim 4$  turnovers):

(i) A simple balance between turbulent transport and burning in the convection zone is maintained, whereby any amount of material entrained into the convection zone is counterbalanced by nuclear burning (Section 5.3.1; Fig. 6).

(ii) The turbulent composition flux appears to be quasi-static due to a complex balance between turbulent production, nuclear burning, turbulent transport, pressure force coupling, and centrifugal forces (Section 5.3.2; Fig. 7).

(iii) Composition variance provides information about composition fluctuation amplitudes, and the residual of the composition

variance mean field equation then gives direct information about numerical dissipation time-scales (Section 5.3.3).

### 6.3 Dissipation and ILES

The residual of the composition variance equation implies a match with the Kolmogorov damping time-scale (Section 5.3.3; Fig. 8). This independently confirms a similar result found using the turbulent kinetic energy equation (Meakin & Arnett 2007; Arnett et al. 2010), and indicates a deep consistency in our ILES approach. In the simulation, the dissipation of both turbulent kinetic energy and composition variance occurs at the sub-grid level, as desired. This should be true of the entropy and temperature variances as well, because ILES joins on to the inertial range of the turbulent cascade.

### 6.4 Implications for stellar evolution theory

As discussed above (Section 6.1), we have identified very substantial differences between 1D stellar evolution modelling and our 3D modelling. These findings indicate that if shell mergers and entrainment do happen in real stars, 1D evolutionary models that do not include these phenomena are likely to be substantially in error. Moreover, based on our finding of the way in which ingested fuel burns in the convective zone, it appears that even if 1D models do incorporate shell mergers and entrainment, current 1D theory would be unable to model them reliably.

The differences identified here will need to be addressed to improve modelling of convective-reactive phases. If not addressed the errors from these events will accumulate through the subsequent evolutionary phases and will cause uncertainty in, for example, pre-supernova evolution and the 3D explosion models that rely on the 1D models for their initial states.

Further 3D modelling – and, just as importantly, detailed analysis such as that presented in this paper – is vital to guide these improvements by illuminating the physical processes at play.

## ACKNOWLEDGEMENTS

MM acknowledges support of the Los Alamos National Laboratory where he was a postdoctoral research fellow and where much of this research was done. CAM acknowledges support from Los Alamos National Laboratory as well as the University of Arizona. SWC acknowledges federal funding from the Australian Research Council though the Future Fellowship grant entitled ‘Where are the Convective Boundaries in Stars?’ (FT160100046). Part of this work was supported by computational resources provided by the Australian Government through NCI via the National Computational Merit Allocation Scheme (project ew6). WDA acknowledges support from the Theoretical Astrophysics Program (TAP) and Steward Observatory, where these simulations and first analyses were begun. Authors acknowledge Raphael Hirschi for his suggestion of the RA-ILES acronym used to describe our analysis.

## REFERENCES

- Arnett W. D., 1972a, *ApJ*, 176, 681
- Arnett W. D., 1972b, *ApJ*, 176, 699
- Arnett W. D., 1974a, *ApJ*, 193, 169

- Arnett W. D., 1974b, *ApJ*, 194, 373  
 Arnett D., 1996, Supernovae and Nucleosynthesis. Princeton Univ. Press, Princeton, NJ  
 Arnett D., Meakin C., Young P. A., 2009, *ApJ*, 690, 1715  
 Arnett D., Meakin C., Young P. A., 2010, *ApJ*, 710, 1619  
 Arnett W. D., Meakin C., Viallet M., Campbell S. W., Lattanzio J. C., Mocák M., 2015, *ApJ*, 809, 30  
 Besnard D., Harlow F., Rauenzahn R., Zemach C., 1992, Technical Report, Turbulence Transport Equations for Variable-Density Turbulence and Their Relationship to Two-Field Models. Los Alamos National Lab., NM, USA  
 Böhm-Vitense E., 1958, *Zeitschrift für Astrophysik*, 46, 108  
 Campbell S. W., Lattanzio J. C., 2008, *A&A*, 490, 769  
 Caughlan G. R., Fowler W. A., 1988, *At. Data Nucl. Data Tables*, 40, 283  
 Chassaing P., Antonia R., Anselmet F., Joly L., Sarkar R., 2010, Variable Density Fluid Turbulence. Kluwer Academic Publishers, Dordrecht  
 Clayton D. D., 1983, Principles of Stellar Evolution and Nucleosynthesis. University of Chicago Press, Chicago  
 Colella P., Glaz H. M., 1985, *J. Comput. Phys.*, 59, 264  
 Colella P., Woodward P. R., 1984, *J. Comput. Phys.*, 54, 174  
 Cristini A., Meakin C., Hirschi R., Arnett D., Georgy C., Viallet M., Walkington I., 2017, *MNRAS*, 471, 279  
 Dimotakis P. E., 2005, *Annu. Rev. Fluid Mech.*, 37, 329  
 Fox R., 1995, Computational Methods for Turbulent Reacting Flows. Cambridge Univ. Press, New York  
 Fryxell B., Arnett D., Mueller E., 1991, *ApJ*, 367, 619  
 Fujimoto M. Y., Ikeda Y., Iben I., Jr., 2000, *ApJ*, 529, L25  
 Goriely S., Siess L., 2004, *A&A*, 421, L25  
 Grinstein F. F., Margolin L. G., Rider W. J., 2007, Implicit Large Eddy Simulation. Cambridge Univ. Press, Cambridge  
 Herwig F., 2004, *ApJ*, 605, 425  
 Herwig F., Blöcker T., Langer N., Driebe T., 1999, *A&A*, 349, L5  
 Herwig F., Pignatari M., Woodward P. R., Porter D. H., Rockefeller G., Fryer C. L., Bennett M., Hirschi R., 2011, *ApJ*, 727, 89  
 Hinze J. O., 1975, Turbulence, McGraw-Hill Series in Mechanical Engineering, 2nd edn, McGraw-Hill College, New York  
 Landau L. D., Lifshitz E. M., 1959, Fluid Mechanics. Course of Theoretical Physics, Vol. 6. Addison-Wesley, Boston  
 Meakin C. A., 2006, PhD thesis, The University of Arizona, Arizona, USA  
 Meakin C. A., Arnett D., 2007, *ApJ*, 667, 448  
 Mocák M., Müller E., Weiss A., Kifonidis K., 2009, *A&A*, 501, 659  
 Mocák M., Siess L., Müller E., 2011, *A&A*, 533, A53  
 Mocák M., Müller E., Siess L., 2012, in Miglio A., Montalbán J., Noels A., eds, *Hydrodynamic Simulations of Shell Convection in Stellar Cores*, Vol. 26. Red Giants as Probes of the Structure and Evolution of the Milky Way. Astrophysics and Space Science Proceedings. Springer, Berlin, Heidelberg, p. 87  
 Mocák M., Meakin C., Viallet M., Arnett W. D., 2014, preprint ([arXiv: 1401.5176](https://arxiv.org/abs/1401.5176))  
 Pope S. B., 2000, Turbulent Flows. Cambridge Univ. Press, Cambridge  
 Schlattl H., Salaris M., Cassisi S., Weiss A., 2002, *A&A*, 395, 77  
 Stancliffe R. J., Dearborn D. S. P., Lattanzio J. C., Heap S. A., Campbell S. W., 2011, *ApJ*, 742, 121  
 Stein R. F., Nordlund Å., 1998, *ApJ*, 499, 914  
 Sytne I. V., Porter D. H., Woodward P. R., H. H. S., Winkler K. H., 2000, *J. Comput. Phys.*, 158, 224  
 Timmes F. X., Swesty F. D., 2000, *ApJS*, 126, 501  
 Tritton D. J., 1988, Physical Fluid Dynamics, 2 edn. Oxford Univ. Press, Oxford  
 Truran J. W., Arnett W. D., 1970, *ApJ*, 160, 181  
 Viallet M., Meakin C., Arnett D., Mocák M., 2013, *ApJ*, 769, 1  
 Woodward P. R., Herwig F., Lin P.-H., Knox M., Fryer C., 2014, *ApJ*, 792, 3  
 Woodward P. R., Herwig F., Lin P.-H., 2015, *ApJ*, 798, 49  
 Woosley S. E., Heger A., Weaver T. A., 2002, *Rev. Mod. Phys.*, 74, 1015  
 Young P. A., Arnett D., 2005, *ApJ*, 618, 908

## APPENDIX A: APPROXIMATE RATES OF ENERGY GENERATION

The nuclear burning of carbon, neon, oxygen, and silicon during advanced evolutionary stages of massive stars involve increasingly extensive nuclear reaction networks, which have been analysed and reduced to much simpler equivalent forms (Arnett 1996). These equivalent nuclear reactions (see Arnett 1972a,b, 1974a; Arnett 1974b for original work), allow calculation of approximate formulas for nuclear energy production rates coming from each of these equivalent reaction links, and are useful for understanding the energy generation. Our simulations actually use the 25-species network in each zone. Here, we give simpler approximations which are useful for analysis; see Fig. 5.

Nuclear energy production due to  $^{12}\text{C}$  burning goes primarily to unstable highly excited state of  $^{24}\text{Mg}$  which decays further through neutron,  $\alpha$ , and proton channel to  $\text{Mg}^{23}$ ,  $^{20}\text{Ne}$ , and  $\text{Na}^{23}$  and its rate (in  $\text{erg g}^{-1} \text{s}^{-1}$ ) can be approximated by Arnett (1972b):

$$\dot{\epsilon}_{c12}^{\text{nuc}} \approx 4.8 \times 10^{18} Y_{c12}^2 \rho \lambda_{c12,c12}, \quad (\text{A1})$$

where  $\lambda_{c12,c12}$  is reaction rate for  $^{12}\text{C}(^{12}\text{C}, \gamma)^{24}\text{Mg}$  Caughlan & Fowler (1988).

Neon burns in massive stars primarily by reaction  $^{20}\text{Ne}^{20} \rightarrow ^{16}\text{O} + ^{24}\text{Mg}$ , assuming approximate equilibrium between one photo-disintegrated  $^{20}\text{Ne}$  into  $^{16}\text{O}$  and  $^4\text{He}$  and one  $\alpha$  capture on the new oxygen restoring  $^{20}\text{Ne}$ . At this point, one  $^4\text{He}$  starts to add to  $^{20}\text{Ne}$  and produces  $^{24}\text{Mg}$ . The net effect is that for each two neon nuclei there is one new nucleus of  $^{16}\text{O}$  and one of  $^{24}\text{Mg}$  produced. Its nuclear production rate (in  $\text{erg g}^{-1} \text{s}^{-1}$ ) can be approximated by Arnett (1974a):

$$\dot{\epsilon}_{ne20}^{\text{nuc}} \approx 2.5 \times 10^{29} T_9^{(3/2)} \frac{Y_{ne20}^2}{Y_{o16}} \lambda_{ne20}^{\alpha\gamma} e^{-(54.89/T_9)}, \quad (\text{A2})$$

where  $\lambda_{ne20}^{\alpha\gamma}$  is the reaction rate for  $^{20}\text{Ne}(\alpha, \gamma)^{24}\text{Mg}$  Caughlan & Fowler (1988) and  $T_9$  is temperature  $T$  divided by  $10^9\text{K}$ . The equilibrium in the neon burning holds in our network, as indicated by a proximity of the neon nuclear time-scales for  $\text{Ne}^{20} \rightarrow \text{He}^4 + \text{O}^{16}$  and  $\text{He}^4 + \text{O}^{16} \rightarrow \text{Ne}^{20}$  shown in Fig. 5.

Oxygen burning produces compound nuclear states of  $^{32}\text{S}$ , which may decay by neutron, proton, deuteron or  $\alpha$  channel into  $^{31}\text{S}$ ,  $^{31}\text{P}$ ,  $^{30}\text{P}$ , or  $^{28}\text{Si}$  but the  $n$ ,  $p$ , and  $\alpha$  are recaptured, giving a distribution of nuclei from  $^{28}\text{Si}$  to Ca isotopes (Truran & Arnett 1970; Arnett 1974b). The energy production rate (in  $\text{erg g}^{-1} \text{s}^{-1}$ ) can be approximated by:

$$\dot{\epsilon}_{o16}^{\text{nuc}} \approx 8 \times 10^{18} Y_{o16}^2 \rho \lambda_{o16,o16}, \quad (\text{A3})$$

where  $\lambda_{o16,o16}$  is reaction rate for  $^{16}\text{O}(^{16}\text{O}, \gamma)^{32}\text{S}$  Caughlan & Fowler (1988).

Simplified view of silicon burning involves two nuclei of  $^{28}\text{Si}$  producing one  $^{56}\text{Ni}$  nucleus via specific sequence of photo-disintegration and fusion reactions. The critical reaction that allows the photo-disintegration of  $^{28}\text{Si}$  is  $^{24}\text{Mg}(\gamma, \alpha)^{20}\text{Ne}$ . The energy production rate can during such silicon burning be approximated by

$$\dot{\epsilon}_{si28}^{\text{nuc}} \approx 1.8 \times 10^{28} T_9^{3/2} X_{si28} \lambda_{ne20}^{\alpha\gamma} e^{-142.07/T_9} \quad (\text{A4})$$

(Clayton 1983; Woosley, Heger & Weaver 2002).